



Die Grenzen der
Chemie neu ausloten?
It takes
#HumanChemistry

Wir suchen kreative Chemikerinnen und Chemiker,
die mit uns gemeinsam neue Wege gehen wollen –
mit Fachwissen, Unternehmertum und Kreativität für
innovative Lösungen. Informieren Sie sich unter:

[evonik.de/karriere](https://www.evonik.de/karriere)

Organic Semiconductor/Insulator Blends for Elastic Field-Effect Transistors and Sensors

Lukasz Janasz, Michal Borkowski, Paul W. M. Blom, Tomasz Marszalek, and Wojciech Pisula*

Organic semiconductors encounter limitations in their practical applicability in future electronics due to their low environmental stability and poor charge carrier mobilities. Blending with isolation of thermoplastic polymers and elastomers circumvents these restrictions and even induces new material properties, opening the door to novel flexible and stretchable electronics that hold great potential for improving people's life. This review discusses next generation applications of solution processable organic semiconductor/insulator blends in organic field-effect transistors (OFETs). The fundamental basis is a comprehensive understanding of the phase separation mechanism that determines the morphology formation and electronic properties of the thin blend film. Continuous charge carrier pathways in blend OFETs are established by controlled phase separation through the chemical structure of components and the processing conditions. Recent advances in organic semiconductor/insulator blends with enhanced device properties including charge carrier mobility, life-time, sensing ability, and especially mechanical behavior are reviewed with emphasis on implication in flexible and stretchable electronics. The concept of tuning existing properties and creating new ones of electronically active materials by blending with well-selected insulators has great potential also for other types of electronic devices and classes of semiconductors.

several important challenges must be overcome. This includes enhancement of the charge carrier transport and environmental stability of organic semiconductors that consist of conjugated polymers and small molecules.^[5–7] Inorganic semiconductors, like crystalline silicon, still outperform organic semiconductors in device performance, especially in field-effect transistors (FETs).^[8,9] In crystalline inorganic semiconductors, electrons are efficiently transported and their motion can be theoretically described by band transport and Bloch theory. As a drawback, the conventional wafer-based technology is unsuitable for mechanically flexible or stretchable applications because of inherent brittleness and rigidity of the inorganic semiconductor. The molecular order and thin film microstructure of organic semiconductors is significantly more disordered. Due to amorphous or semicrystalline order, the charge carrier transport is mostly determined by hopping between localized states, and is less efficient than in highly crystalline inorganic

1. Introduction

Organic electronic devices, despite being rapidly developed in the last decades, still require further improvements to meet the expectations of the modern electronic industry.^[1–4] Before full-scale commercialization of organic electronics is possible,

semiconductors.^[10,11] Since the molecules are held together by weak van der Waals and π - π non-covalent forces, organic semiconductors exhibit a lower tensile modulus than crystalline inorganic ones, making them suitable for mechanically flexible and stretchable electronics.^[12–17] Simple and cost-effective solution processing of soluble organic semiconductors into large area films is another essential advantage which cannot be achieved with traditional inorganic systems.^[18,19]

L. Janasz, M. Borkowski, T. Marszalek, W. Pisula
Department of Molecular Physics
Faculty of Chemistry
Lodz University of Technology
Zeromskiego 116, Lodz 90-924, Poland
E-mail: pisula@mpip-mainz.mpg.de
Paul W. M. Blom, T. Marszalek, W. Pisula
Department of Molecular Electronics
Max Planck Institute for Polymer Research
Ackermannweg 10, 55128 Mainz, Germany

 The ORCID identification number(s) for the author(s) of this article can be found under <https://doi.org/10.1002/adfm.202105456>.

© 2021 The Authors. Advanced Functional Materials published by Wiley-VCH GmbH. This is an open access article under the terms of the Creative Commons Attribution License, which permits use, distribution and reproduction in any medium, provided the original work is properly cited.

DOI: 10.1002/adfm.202105456

Stretchability and flexibility is attractive for electronic components applied in medical diagnostics that are in contact with the human body.^[20,21] Flexible and stretchable circuits can be placed as sensors directly on the patient's skin or even organs, such as heart, during surgery to monitor the life functions.^[22] These applications are feasible as the tensile modulus of organic semiconductors can be tailored to match the mechanical elasticity of the human skin.^[23] Applications of flexible and stretchable electronics are not limited to medicine or bio-sciences, but can also be embedded in smart-clothes, bendable displays, or solar panels.^[24,25]

An efficient way to improve mechanical flexibility or stretchability of organic semiconducting films is mixing the conjugated molecules with materials of lower tensile modulus.^[26] Insulating polymers with conductivity below $10^{-8} \Omega^{-1} \text{ cm}^{-1}$, like polydimethylsiloxane (PDMS) elastomer or thermoplastic

polystyrene (PS), serves as the matrix for the organic semiconductor molecules forming together the active blend film.^[27] Interestingly, blends with large majority of the insulator and appropriate morphology can show even a higher charge carrier mobility than the pure semiconductor.^[28,29] The phase separation between insulator and organic semiconductor can lead to a bilayer structure and in this way, additionally to an encapsulation of the active layer ensuring a higher environmental stability of the organic field-effect transistors (OFETs).^[30,31] Mixing a minor amount of the organic semiconductor with large excess of the insulator is also a smart way to reduce usage of expensive compounds and to decrease costs of organic electronic devices.

In this review, we address recent advances on OFETs based on organic semiconductor–insulator blends (Table 1). Especially the improvement in charge carrier transport and environmental stability is emphasized with a link to novel properties and functions of the devices, such as mechanical flexibility, stretchability, and sensing. The focus is drawn on transistors for two main reasons: i) development of OFETs is crucial for the progress of organic electronics in general, since transistors are basic building blocks in logic circuits, and ii) OFETs are a powerful experimental tool to gain insight into the correlation between structural properties and charge carrier transport of the semiconducting film. This includes the description of the phase separation mechanism between semiconductor and insulator (Section 2) and the resulting advantages for the device functionality (Section 3) for both types of organic semiconductors, conjugated polymers, and small molecules. The device encapsulation driven by phase separation for enhancing the environmental stability is described in Section 4. In the final Sections 5 and 6, key functionalities of blend OFETs comprising mechanical flexibility, stretchability, and sensing for novel technologies, are discussed.

2. Phase Separation Mechanism

Mixing an organic semiconductor with high excess of an insulator polymer can be expected to significantly deteriorate the charge carrier transport because the non-conducting matrix in the active film results in conductivity reduction. Interestingly, at certain circumstances, the charge carrier transport in blend films does not decline but is even improved in comparison to the neat semiconductor. A prerequisite for an efficient charge transport in blends is a well-defined phase separation between the organic semiconductor and insulator.^[32,33] A further requirement is a particular blend morphology allowing the formation of percolation pathways for charge carriers.^[34–36] The term morphology describes the arrangement of molecules in the solidified thin film on a large scale. It encloses high level order such as fibrillar structures and defines the phase separation in blends. Such morphology can be comprised of continuous, in-plane arranged semiconducting pathways exceeding tenths of micrometers to interconnect the source and drain electrodes in the transistor. An unfavorable film microstructure consists of individual small semiconductor domains separated from each other within the insulating matrix.

The phase separation between organic semiconductor and polymer insulator is governed by the Gibbs free energy of

mixing. Its change upon mixing is expressed according to the following formula:

$$\Delta G_m = \Delta H_m - T\Delta S_m \quad (1)$$

where ΔH_m and ΔS_m are enthalpy and entropy of mixing, and T is the temperature. Positive and high ΔG_m enhances phase separation. The Flory–Huggins theory introduces the parameter, χ which describes the interaction between mixed molecules:

$$\chi_{1-2} = \frac{V_1 (\delta_1 - \delta_2)^2}{RT} + 0.34 \quad (2)$$

where V_1 is the molar volume of the solvent and δ_1 and δ_2 are solubility parameters of the solvent and solute, respectively. Estimation of the solubility parameters of the semiconductor and the insulator, followed by calculations of the interaction parameter χ and ΔG_m are valuable for the right choice of compounds and concentrations for a favorable phase separation. For instance, a high molecular weight (M_w) of the insulator decreases the entropy of mixing and according to Equation (1), increases ΔG_m intensifying the tendency toward phase separation. For example, ΔG_m was estimated for the mixture of 6,13-bis(triisopropyl-silylethynyl)-pentacene (TIPS-pentacene) and insulating poly(α -methylstyrene) (P α MS).^[37] While ΔG_m was negative for the blend with low M_w P α MS (2 kDa) indicating a small tendency toward phase separation, the value became positive when the same dielectric polymer was applied with much higher M_w (100 kDa). Time-of-flight secondary ion mass spectrometry (TOF–SIMS) revealed that spin-cast films of both blends a uniform distribution of semiconducting and insulating molecules within the layer profile in the case of low M_w P α MS, and a phase separated trilayer for high M_w P α MS (Figure 1a).

The mass ratio between insulator and semiconductor also affects ΔG_m and the propensity for phase separation. According to the above-mentioned Flory–Huggins theory, the relation between ΔG_m and concentration is given by the following equation:

$$\Delta G_m = RT \left(\varphi_0 \ln \varphi_0 + \ln \varphi \sum_i \frac{\varphi_i}{m_i} + \varphi_0 \varphi \chi \right) \quad (3)$$

$$\varphi = \sum_i \varphi_i = 1 - \varphi_0 \quad (4)$$

Where φ_0 is the volume fraction of the solvent, φ_i is the volume fraction of one solute, and m_i is a quantity proportional to the degree of polymerization of one solute. For instance, the optimal weight ratio for phase separation of TIPS-pentacene and poly[bisphenol A carbonate-co-4,40-(3,3,5-trimethylcyclohexylidene)diphenol carbonate] (APC) was determined as 1:4, by calculating ΔG_m (Figure 1b).^[38] Inkjet printed films of this blend ratio formed a strong lateral phase separation between the polymer phase and TIPS-pentacene stripe-shaped crystals that contributed to the highest charge carrier mobility among other blend ratios within this series.

The evaluation of ΔG_m is valuable to predict the tendency for phase separation in a semiconductor–insulator blend. However,

Table 1. Summary of the key organic semiconductor–insulator blends with their main properties discussed in this review.

Organic semiconductor	Organic insulator	Phase separated morphology	Phase separation mechanism	Application	Charge carrier mobility [cm ² V ⁻¹ s ⁻¹]	Application specific performance	Reference
TIPS-pentacene	PαMS	Vertical; trilayer Top and bottom semiconductor; middle insulator	High <i>M_w</i> of insulator leading to high delta G _m	Rigid OFET	10 ⁻¹		[37]
	PαMS	Vertical; trilayer Top and bottom semiconductor; middle insulator	Solute–solute interactions	Rigid OFET	0.3		[46]
	PαMS	Vertical Top semiconductor; bottom insulator	Prolonged drying time enhanced semiconductor crystallization	Rigid OFET	1.3		[67]
	APC	Lateral Stripe-shaped crystallized semiconductor	Insulator / semiconductor weight ratio optimized for high G _m	Rigid OFET	0.5		[38]
	PS	Lateral Stripe-shaped crystallized semiconductor	Prolonged drying time enhanced semiconductor crystallization	Rigid OFET	1.3		[62]
	PS	Vertical Top semiconductor; bottom insulator	High <i>M_w</i> of insulator leading semiconductor crystallization during shear coating	Rigid OFET	12.3		[68]
	PS	Vertical; trilayer Top and bottom insulator; middle semiconductor	Low viscosity and prolonged drying time of solution	Rigid OFET	0.7	Environmental device stability after 390 days due to encapsulation	[62]
	iPS	Vertical; trilayer Top and bottom semiconductor; middle insulator	Semiconductor and insulator crystallization sequence	Rigid OFET	0.03		[66]
	PS	Lateral	Solute–solute interactions	Gas sensor (NH ₃)	0.6	Detection limit 5 ppm Ultra-low DC power consumption of 50 nW	[138]
	PS	Vertical Top semiconductor; bottom insulator	Solute–solute interactions	Gas sensor (NH ₃)	0.65	Sensitivity of 0.06 (defined as Δ <i>I_{DRAIN}</i> / <i>I₀</i>)	[139]
DiF–TES–ADT	PMMA	Vertical; trilayer; Top and bottom insulator; middle semiconductor	Low viscosity and prolonged drying time of solution	Rigid OFET	0.3	Environmental device stability after 390 days due to encapsulation	[62]
	PαMS	Vertical; trilayer Top and bottom insulator; middle semiconductor	Entropy driven due to high <i>M_w</i> of insulator	Rigid OFET	10 ⁻¹		[64]
	PαMS	Vertical Top semiconductor; bottom insulator	High <i>M_w</i> of insulator leading to semiconductor crystallization during shear coating	Rigid OFET	4.5		[69]
	PS	Vertical Top semiconductor; bottom insulator	High <i>M_w</i> of insulator leading to semiconductor crystallization during shear coating	Rigid OFET	1.2		[69]
	PS	Lateral	Solute–substrate interactions	Pressure sensor		Sensitivity of 1.07 kPa Relaxation time of 18 ms at pressure of 1.0 kPa and frequency of 0.5 Hz	[144]
PMMA	Vertical Top semiconductor; bottom insulator	Solute–substrate interactions	Rigid OFET	10 ⁻³		[64]	

Table 1. Continued.

Organic semiconductor	Organic insulator	Phase separated morphology	Phase separation mechanism	Application	Charge carrier mobility [cm ² V ⁻¹ s ⁻¹]	Application specific performance	Reference
Rubrene	P4VP	Vertical Top semiconductor; bottom insulator	Solute–solvent and solute–substrate interactions	Rigid OFET	0.52		[75]
	PS	Vertical Top semiconductor; bottom insulator	Solute–solvent and solute– substrate interactions	Rigid OFET	0.07		[75]
C8-BTBT	PS	Vertical Top semiconductor; bottom insulator	Solute–substrate interactions	Rigid OFET	6.8	Environmental device stability	[63]
	PS	Vertical; trilayer Top and bottom insulator; middle semiconductor	Crystallization driven separation	Rigid OFET	10 ⁻²	Structural stability after 420 -days of environmental exposure due to encapsulation	[34]
C5-BTBT	PI	Lateral	Solute–solute interactions	UV sensor (365 nm)		Light detection limit of 0.12 mW cm ⁻² ; photosensitivity of 10 ⁶ (<i>I</i> _{light} / <i>I</i> _{dark}); Photo responsivity of 429 AW ⁻¹	[142]
	PI	Lateral	Solute–solute interactions	UV sensor (365 nm)		Light detection limit of 0.11 mW cm ⁻² ; photosensitivity of 10 ⁷ (<i>I</i> _{light} / <i>I</i> _{dark}); Photoresponsivity of 67 AW ⁻¹	[143]
PDIC8CN2	PS	Vertical; trilayer Top and bottom insulator; middle semiconductor		Rigid OFET	10 ⁻²	Device stability after 150 days of environmental exposure due to encapsulation	[30]
P3HT	PDMS	Vertical Top insulator; bottom semiconductor fibers	Solute–substrate and solute– solute interactions	Stretchable OFET	7.82 × 10 ⁻³	Device stability up to 100% elongation	[44]
	PDMS	Vertical Top insulator; bottom semiconductor fibers	Solute–solute, solute– surface interactions and semiconductor aggregation	Stretchable OFET	0.24	Device stability up to 100% elongation	[116]
	PDMS	Vertical Top insulator; bottom semiconductor fibers	Semiconductor aggregation and precipitation in solution	Stretchable OFET	0.07	Device stability up to 62% elongation	[107]
	PMMA	Vertical Top semiconductor; bottom insulator	Solute–substrate interactions	Flexible, self- standing OFET	0.02	Stability as self-standing device	[121]
	PMMA	Vertical Top semiconductor; bottom insulator	Solute–substrate interactions	Gas sensor (NO ₂)		Responsivity of 1481% and 487% at 30 ppm and 0.5 ppm of NO ₂ NO ₂ detection limit of 0.7 ppb	[136]
	PMMA	Vertical Top semiconductor; bottom insulator	Solute–substrate interactions	Gas sensor (NH ₃)	2.3 × 10 ⁻²	Responsivity of 31.1% for 2 nm thick active film at 10 ppm of NH ₃	[146]
	PS	Interpenetrating bicontinuous network	Spinodal decomposition	Rigid OFET	10 ⁻³		[78]
	PS	Interpenetrating network Semiconductor fibrils in insulating matrix	Preaggregation of semiconductor in solution	Semiconducting film		Conductivity of 10 ⁻⁴ S cm ⁻¹	[79]
	PS	Vertical Top semiconductor fibrils; bottom insulator	Preaggregation, solute– substrate and solute–solvent interactions	Rigid OFET	10 ⁻²		[80]

Table 1. Continued.

Organic semiconductor	Organic insulator	Phase separated morphology	Phase separation mechanism	Application	Charge carrier mobility [cm ² V ⁻¹ s ⁻¹]	Application specific performance	Reference
	PS	Vertical Top semiconductor fibrils; bottom insulator	Solute–substrate and solute–solvent interactions	OFET and digital inverter	1.3	Leakage current of 10 ⁷ mA cm ⁻¹	[84]
	PS	Vertical Top insulator; bottom semiconductor	Semiconductor aggregation in solution and solute– solvent interactions	Rigid OFET	0.08	Device stability after 7 days environmental exposure due to encapsulation	[81]
	PS	Lateral	Solute–substrate interactions	Gas sensor (NH ₃)		Responsivity of 52% and 16% at 50 ppm and 5 ppm of NH ₃	[145]
	PS	Lateral	Solute–solute interactions	Gas sensor (NO ₂)		Sensitivity of 48.2% per every ppm of NO ₂ Responsivity of 20 000% at 20 ppm of NO ₂ Switching speed 4.7 s	[130]
	HDPE	Vertical Top insulator; bottom semiconductor	Insulator and semiconductor crystallization sequence	Rigid OFET	10 ⁻²	Encapsulated device	[42]
	PE	Lateral	Solute–solute interactions	Reversible thermo- responsive OFET		30% mobility decline when temperature increased from 30 °C to 120 °C	[129]
	MEH-PPV	Interpenetrating bicontinuous network	Spinodal decomposition	Rigid OFET	10 ⁻³		[78]
	Paraffin	Vertical Top insulator; bottom semiconductor	Semiconductor aggregation in solution	Rigid OFET	0.072	Device stability after 28 days environmental exposure due to encapsulation	[107]
	Paraffin	Vertical Top insulator; bottom semiconductor fibers	Semiconductor aggregation and precipitation in solution	Stretchable OFET	0.07	Device stability up to 50% elongation	[107]
	SEBS	Vertical Top insulator; bottom semiconductor fibers	Solute–solvent and solute–substrate interactions	Stretchable OFET	0.7	Device stability up to 50% elongation	[120]
P3HT-b-PHA	PMMA	Lateral Microphase separation	Solute–solute interactions	UV sensor (254 nm)		Responsivity of 120 AW ⁻¹ <i>I</i> _{light} / <i>I</i> _{dark} ratio of 4000 External quantum efficiency of 4.97 × 10 ⁴	[149]
Polytelluro- phenes	HDPE	Lateral Semiconductor fibrils in insulating spheroids	Solute–solute interactions	Rigid OFET	5.7 × 10 ⁻³		[86]
DPP–DTT	PS	Interpenetrating network Semiconductor fibrils in insulating matrix	Solute–solute interactions and film annealing	Rigid OFET	8.0		[88]
PCDTPT	PS	Vertical Top semiconductor; bottom insulator	Solute – solute and solute – solvent interactions	Transparent OFET	0.5	Optical transparency > 90%	[94]
	PS	Vertical Top insulator; bottom semiconductor	Solute–substrate interac- tions, nanogrooved surface	Rigid OFET	2.7		[90]
	PS	Interpenetrating network Unidirectional semiconductor fibrils in insulating matrix	Solute–substrate interactions, nanogrooved surface	Rigid OFET	23		[91]
PF	PS	Lateral	Solute–solute interactions	Photonic transistor memory		Write / erase time of 1s Retention time > 3 months	[95]
PQT	PMMA	Vertical Bottom semiconductor; top insulator	Solute–solvent interactions	Rigid OFET	0.04	Device stability after 48h environmental exposure due to encapsulation	[43]

Table 1. Continued.

Organic semiconductor	Organic insulator	Phase separated morphology	Phase separation mechanism	Application	Charge carrier mobility [cm ² V ⁻¹ s ⁻¹]	Application specific performance	Reference
DPP6T	PMMA	Vertical Top semiconductor; bottom insulator	Viscosity gradient during dip-coating	Rigid OFET	0.6		[65]
DB-TTF	PS	Vertical Top semiconductor; bottom insulator	Solute – substrate interactions	flexible OFET	0.2	Bending radius of 5 mm	[71]
	PS	Vertical Top semiconductor; bottom insulator	Crystallization kinetics and thermodynamics	Rigid OFET	0.2		[76]
29-DPP-TVT	PMMA	Vertical Top insulator; bottom semiconductor	Solute–substrate interactions, Marangoni-instability	Rigid OFET	0.7		[93]
DH4T	PMMA	Vertical Top semiconductor; bottom Insulator	Viscosity gradient during dip-coating	Rigid OFET	0.1		[65]
P-(NDI2OD-T2)	PS	Interpenetrating network Semiconductor short fibrils in insulating matrix	Solute–solute interactions	Rigid and transparent OFET	0.15	Transparency of 85% Transmission over the polymer absorption window	[89]
C8O-BTBT-OC8	PS	Vertical Top semiconductor; bottom insulator	Solute–substrate interactions driven by M _w of the insulator	Rigid OFET	0.9		[77]
PDPP3T	PS	Interpenetrating network Semiconductor fibrils in insulating matrix	Solute–solute interactions	Rigid and transparent OFET	1.5	Transparency of 90% Transmission over the polymer absorption window	[89]
DPP2T	PS	Interpenetrating network Semiconductor fibrils in insulating matrix	Solute–solute interactions (immiscibility)	Flexible OFET	3.1	Device stability after 1000 bending cycles at 5 mm radius	[122]
DPPT-TT	SEBS	Vertical; trilayer Top and bottom semiconductor fibers; middle insulator		Stretchable OFET	1.0	Device stability up to 100% elongation	[123]
DPP-TVT	PDMS	Interpenetrating network Aggregated semiconductor in insulating matrix	Differences in surface energies and thermal annealing	Stretchable OFET	0.1	Device stability after recovery from 100% elongation	[124]
DPP-TVT	BR	Interpenetrating network Semiconductor fibrils in insulating matrix	Solute–solute interactions	Stretchable OFET	0.16 0.043	Device stability up to 100% elongation After self-healing and 50% elongation	[125]
PBIBDF-BT	PBA	Lateral	Solute–solute interactions	Humidity sensor		Sensitivity ratio of 415 at range of 32% TH to 69% RH Recovery time of 45 s	[151]
PBIBDF-BT	PBA	Lateral	Solute–solute interactions	Gas sensor (NH ₃)		Response time < 1s Detection limit of 0.5 ppm Sensitivity of 800 at 10 ppm NH ₃	[152]
PBTIDBIBDF-5	PBA	Lateral	Solute–solute interactions	Photo sensor		Detection limit of 0.03 mW cm ⁻² Responsivity of 128 AW ⁻¹	[153]

the morphology of the blend film is an outcome of various physicochemical factors that occur during the film casting and solidification process.^[39] Depending on the blend components, casting and post-treatment conditions, lateral or vertical phase separation arises.^[31,40] The vertical phase separation

leads to bilayer structures with the semiconductor layer at the top or bottom of the film, or even a trilayer morphology with the insulator between two semiconductor-rich regions. Three types of interactions that govern the phase separation between insulator and semiconductor are distinguished: solute–solvent,

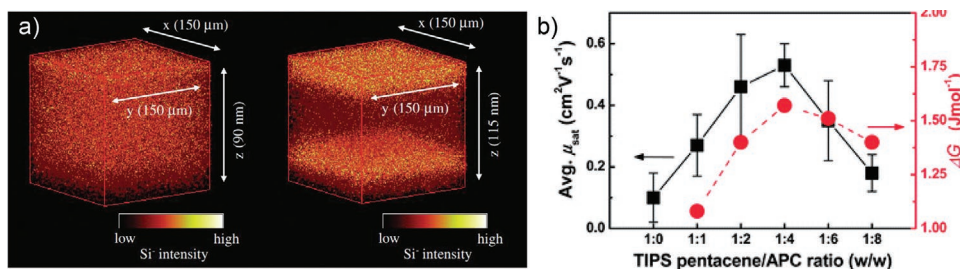


Figure 1. a) Distribution of Si⁻ ions (indicating presence of TIPS-pentacene) in TIPS-pentacene-P α MS blends with high (right) and low (left) M_w P α MS insulator. Reproduced with permission.^[37] Copyright 2009, The Japan Society of Applied Physics. b) Charge carrier mobility and ΔG_m of TIPS-pentacene-APC blends with different weight ratios. Reproduced with permission.^[38] Copyright 2013, The Royal Society of Chemistry.

solute–substrate, and solute–solute.^[32] Interplay between these three types of molecular interactions results in a specific morphology of the solidified semiconductor–insulator film (Figure 2a).

After deposition from a homogenous solution, the phase separation mechanism in multicomponent systems follows three scenarios during the solidification process via solvent evaporation as displayed in the diagram in Figure 2b: i) crystallization by nucleation and growth, ii) binodal, or iii) spinodal decomposition.^[39,41] The first step during crystallization is a primary nucleation where stable nuclei initiated by heterogeneous or homogenous nucleation are formed. The nucleation and crystallization mechanism depends on temperature^[42] and thus on evaporation rate of the solvent influencing the concentration of the solute. When the multicomponent system reaches the upper or lower critical solution temperature, the single stable phase changes to the metastable or unstable region. This relates to the appearance of two local energetic minima, which results in an energetic benefit for the system to undergo phase separation. The solute–solvent, solute–substrate, and solute–solute interactions may decide whether the phase separation is directed by crystallization or spinodal decomposition.

Solute–solvent interactions induce phase separation due to differences in solubility between semiconductor and insulator in a specific solvent. During casting and solvent evaporation, the concentration of the solutes increases in proximity to the solution/air interface. The less soluble compound becomes

even more concentrated at the solution/substrate interface where the solvent concentration is less affected by evaporation. This effect was observed for a vertical phase separation between semiconducting poly[5,50-bis(3-dodecyl-2-thienyl)-2,20-bithiophene] (PQT) and insulating poly(methyl methacrylate) (PMMA) in films deposited from 1,2 dichlorobenzene (DCB).^[43] Because of its lower solubility, PQT solidified as the first compound at the solution/substrate, while PMMA formed the subsequent upper layer.

Solute–substrate interactions initiate phase separation owing to differences in adhesive forces of the dissolved components to the substrate surface. Compounds with a higher surface energy tend to solidify first at the surface to form the bottom layer. This principle was applied for vertically phase separated films of poly(3-hexylthiophene) (P3HT) and PDMS elastomer. P3HT of higher surface energy formed the bottom layer on a SiO₂ surface, while PDMS created the upper one.^[44] After peeling off the film from the rigid Si/SiO₂ substrate, the elastic bilayer structures were applied in stretchable transistors that are described in more detail later in this review. This methodology is applicable also to small molecules as proven for the blend of 2,7-dioctyl[1]benzothieno[3,2-b][1]benzothiophene (C8-BTBT) and PS.^[45] Favorable enthalpic interactions between PS and the SiO₂ surface are responsible for a preferential sedimentation of the polymer toward the substrate, while the more hydrophobic C8-BTBT molecules crystallize at the top air/film interface. The bilayer morphology with large domains and smooth grain boundaries prevented a dewetting of C8-BTBT from the SiO₂

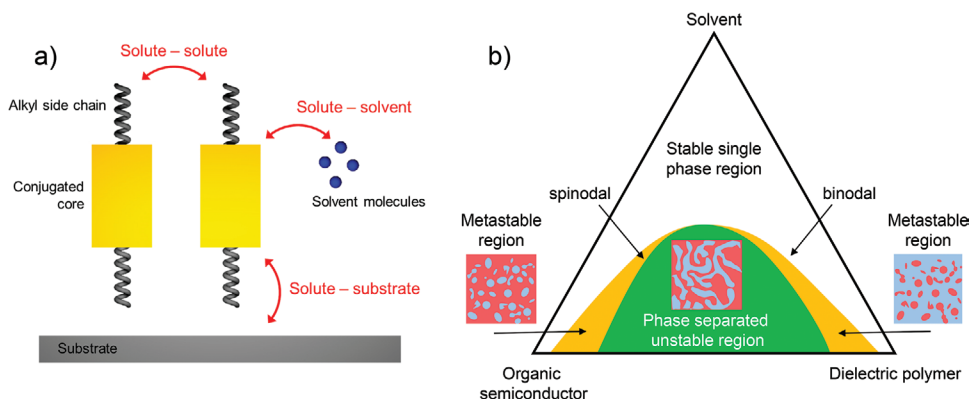


Figure 2. a) Schematic illustration of solute–solvent, solute–substrate, and solute–solute interactions influencing the blend morphology in thin films, b) representative example of a ternary phase diagram for an organic semiconductor:dielectric polymer:solvent multicomponent system. The yellow area indicates the metastable and the green one, the phase separated unstable region.

substrate and ensured environmental stability and charge carrier mobility of $6.80 \text{ cm}^2 \text{ V}^{-1} \text{ s}^{-1}$ of the OFETs.

Solute–solute interactions impact the phase separation when at least one of the components crystallizes. The sequence of crystallization is thereby especially important governing the layer order in vertically phase separated films. A well-known example is the trilayer structure obtained from a blend of crystalline TIPS-pentacene and amorphous P α MS.^[46] Crystalline domains of TIPS-pentacene were expelled from the P α MS matrix prior to its solidification and formed semiconducting-rich areas near the air interface as the upper layer and near the substrate as the bottom layer. This phenomenon was investigated for P α MS with different glass transition temperatures (T_g). It was proven that no phase separation occurred when TIPS-pentacene was blended with P α MS of $T_g = 74 \text{ }^\circ\text{C}$. After annealing the film above $100 \text{ }^\circ\text{C}$, the insulator became viscoelastic allowing TIPS-pentacene molecules sufficient mobility to segregate and to crystallize at the air and substrate interfaces.

Besides the three described concepts, novel approaches have been also developed to control the phase separation. For example, phase separation between P3HT and PMMA was triggered by applying an external electric field during film solidification.^[47] In the electric field, the rearrangement of the π -orbitals induced a motion of P3HT polymer chains creating an efficient phase separation in the blend. The phase separation in semiconductor–insulator blends is a complex process and a prediction of most interactions at specific processing conditions is challenging. A film morphology with a suitable phase separation for efficient charge carrier transport remains mainly an empirical issue supported only to some degree by theoretical predictions.^[48] The physico–chemical theory on phase separation has been described in great detail in literature.^[49,50] For this reason, this review focuses on experimental examples highlighting the potential of semiconductor–insulator blends for flexible and stretchable OFETs in future applications.

3. Charge Carrier Transport in Semiconductor–Insulator Blends

3.1. Charge Carrier Transport in Organic Semiconductors

The charge carrier transport in organic semiconductors is governed to a significant degree by the organization of the conjugated molecules.^[51–53] Charge carriers move along delocalized π -orbitals over the conjugated segments of single molecules and between adjacent molecules via π – π orbital overlap. The transport is strongly affected by the level of dynamic and static disorder.^[11,54] High disorder disrupts the percolation pathways for the charge carriers and decreases the hopping transport. In this case, charges need to overcome potential barriers between adjacent chromophores in order to maintain their motion along the external electric field. The molecular order can be improved by optimization of the deposition and post-treatment conditions.^[55–57] Highly crystalline films of small conjugated molecules sometimes exhibit band transport instead of hopping and charge carrier mobilities exceeding values associated with amorphous silicon.^[52,58] Correspondingly, conjugated polymers with high M_w and high regioregularity also enable efficient

charge carrier transport when ordered structures are formed in the semiconducting film.^[59–61]

3.2. Blends with Small Molecular Semiconductors

At optimized casting and post-treatment conditions, blends of insulating polymer and organic semiconductor can show improved charge carrier transport in comparison to the pristine semiconducting film. In such case, the transport is favored by the blend morphology which comprises a continuous and highly ordered semiconductor phase separated from the insulator. This approach is especially attractive for low M_w semiconductors.^[34,37,62] Low viscosity and dewetting are common drawbacks of small molecules during film casting and blending with insulating polymers enhances their film forming properties.^[63,64] Dip-coated films of α,ω -dihexylquaterthiophene (DH4T) and diketopyrrolopyrrolesexithiophene (DPP6T) exhibited a significant improvement in film formation and crystallization when blended with a small fraction of PMMA.^[65] The film coverage, molecular order, and charge carrier mobility of the semiconductors increased with higher PMMA content and M_w (Figure 3a,b). The blend film morphology consisted of a stratified structure with a continuous thin bottom PMMA layer and highly crystalline ribbons of the organic semiconductor at the top (inset in Figure 3b). The crystallization mechanism was related to PMMA that initiated a viscosity gradient at the meniscus during dip-coating and strengthened in this way, the draw of solute and mass transport (Figure 3c). Additionally, the solidification of the polymer as the bottom layer reduced the nucleation barrier height of the small molecule organic semiconductor (OSC). A similar trend was observed for spin-coated TIPS-pentacene blends. Neat TIPS-pentacene formed during spin-coating gave rise to non-uniform films yielding deviations in the OFET performance.^[46] In contrast, casting blends of TIPS-pentacene and P α MS of high M_w ($\approx 580 \text{ kDa}$) at weight ratio of 1:1 improved the uniformity of the semiconducting phase in the blend film.^[46] The charge carrier mobility increased from $0.03 \text{ cm}^2 \text{ V}^{-1} \text{ s}^{-1}$ for pristine TIPS-pentacene to $0.5 \text{ cm}^2 \text{ V}^{-1} \text{ s}^{-1}$ for the trilayer blend bearing a continuous semiconductor middle layer. Additionally, the device reproducibility was significantly increased.

The crystallinity of the insulating polymer has also a great influence on microstructure and charge carrier transport of TIPS-pentacene in the blend.^[66] While the charge carrier mobility of TIPS-pentacene dropped by two orders of magnitude in blends with elevated excess of low M_w amorphous P α MS, the device performance for blends with semicrystalline iPS remained on an identical level as for the pristine semiconductor. The difference in mobility between the two blends was related to the crystallinity of the insulating polymer. When blended with an amorphous polymer, TIPS-pentacene crystals became disrupted especially at minor semiconductor weight fractions. Below 50% weight fraction of TIPS-pentacene, small and weakly interconnected crystals were well dispersed in the amorphous matrix (Figure 3d). This fine dispersion was attributed to strong interactions between TIPS-pentacene and the amorphous polymer suppressing an efficient phase separation. The poor morphology not only lowered the charge carrier

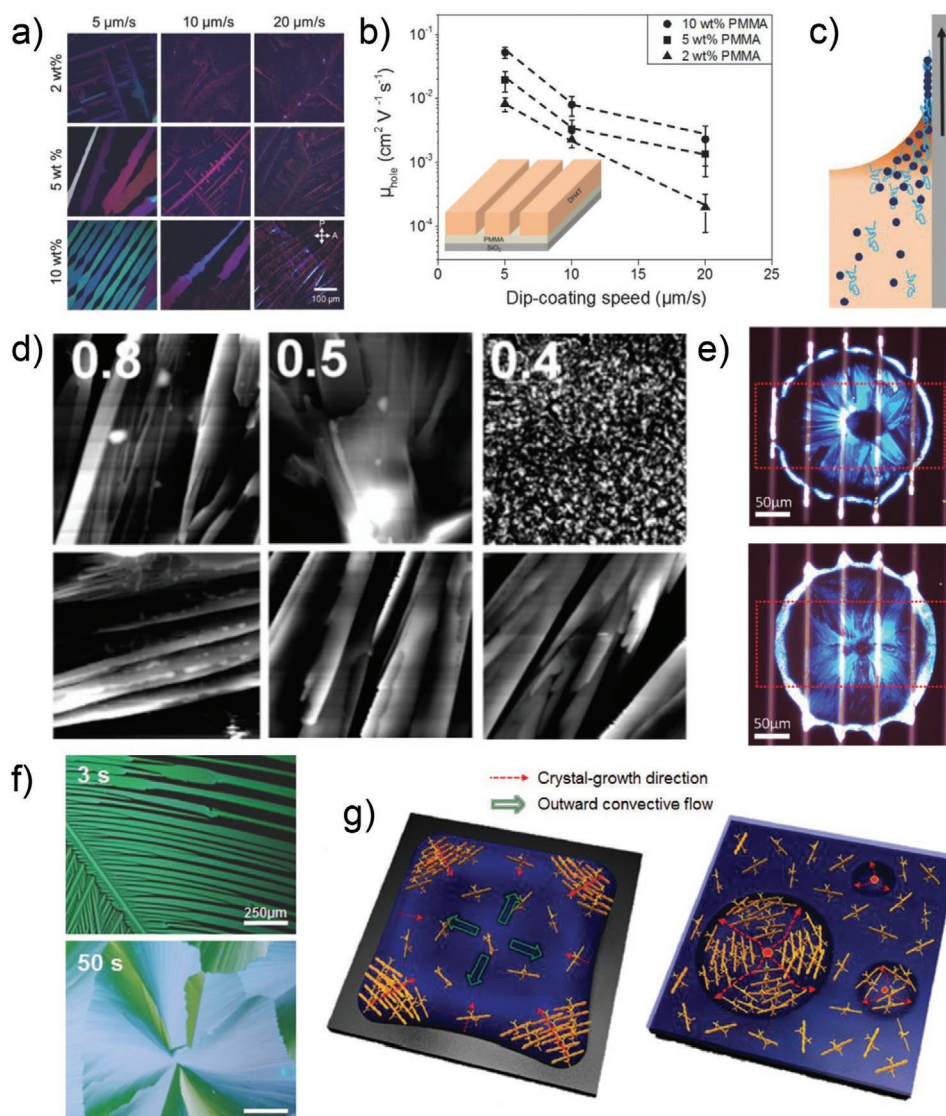


Figure 3. a) Polarized optical microscopy (POM) images and b) hole charge carrier mobility of dip-coated DH4T:PMMA films for various dip-coating speeds and weight fractions of PMMA (inset: illustration of the blend morphology). c) Illustration of the dip-coating mechanism of DH4T:PMMA blends (black dots are DH4T molecules, and blue lines PMMA chains). Reproduced with permission.^[65] Copyright 2018, Wiley-VCH. d) Scanning force microscopy images of TIPS-pentacene films blended with P α MS (upper row) or iPS (lower row) (the inset number indicates weight fraction of the semiconductor in the blend, image size is 20 \times 20 mm²). Reproduced with permission.^[66] Copyright 2008, The Royal Society of Chemistry. e) POM images of inkjet-printed droplet of TIPS-pentacene (upper) and TIPS-pentacene:PS blend (bottom). Reproduced with permission.^[40] Copyright 2011, American Chemical Society. f) POM images of TIPS-pentacene/P α MS blend films spin-cast after 3 s and 50 s, g) illustration of the 1D and 2D crystal growth mechanisms of the spin-coated TIPS-pentacene/polymer blend films. Reproduced with permission.^[67] Copyright 2018, Wiley-VCH.

mobility, but also intensified charge trapping at the grain boundaries as implied by a significant hysteresis in the drain current of the transistor. When TIPS-pentacene was blended with iPS, well-defined crystals with less structural defects (Figure 3d) reduced charge trapping and led to a negligible drain current hysteresis. The drying conditions of the solution coated films also play an essential role in the phase separation and crystallinity of organic semiconductors in the blend. A long drying time induces pronounced order and large TIPS-pentacene domains. The presence of the insulator extends the drying period allowing the molecules to well assemble in crystalline domains.^[40] Extended drying time of inkjet-printed

PS-TIPS-pentacene blends initiated highly separated and ordered film microstructures. A directional alignment of the semiconducting crystals as displayed in Figure 3e enhanced the charge carrier mobility to 0.7 cm² V⁻¹ s⁻¹. In another example, a mobility of 1.3 cm² V⁻¹ s⁻¹ for air-brushed films of TIPS-pentacene and PS was reported.^[62] This device performance was attributed to high TIPS-pentacene crystallinity enforced by slow solvent evaporation and exclusion of impurities from the semiconducting layer during solidification. The drying time did not only enlarge the domain size of TIPS-pentacene in the blends, but also determined the growth mode of the organic semiconductor. It was observed that a great excess of residual solvent

at short spin-coating times stimulated a convective flow in the drying bilayer film followed by a 1 D growth of TIPS-pentacene crystals (Figure 3f,g).^[67] An optimal amount of residual solvent at moderate spin-coating times yielded 2D growth of well-developed TIPS-pentacene spherulites of large coverage, molecular order, and charge carrier mobility (Figure 3f,g). A further rise in OFET performance of TIPS-pentacene was achieved for solution sheared PS blends. The field-effect mobility significantly increased to $12.3 \text{ cm}^2 \text{ V}^{-1} \text{ s}^{-1}$ due to a more preferential molecular packing in vertically phase separated and confined films of continuous and unidirectionally aligned crystalline ribbons.^[68]

Besides TIPS-pentacene, blends of other small conjugated molecules with insulating polymers have also been thoroughly studied. Charge carrier transport in blends of three different insulator polymers mixed with 2,8-difluoro-5,11-bis(triethylsilylethynyl)anthrathiophene (diF-TES-ADT) was investigated.^[64] Two amorphous insulator polymers, high M_w P α MS and PMMA, and one semicrystalline syndiotactic-polystyrene (sPS) were spin-cast with diF-TES-ADT in a 1:1 weight ratio on Si/SiO₂ substrates. The phase separation of diF-TES-ADT with the semicrystalline polymer differed from the behavior of TIPS-pentacene. The weakest phase separation of diF-TES-ADT was observed for crystalline sPS, because the

rapid crystallization of the insulator hampered diffusion and self-assembly of the semiconducting molecules. The diF-TES-ADT/PMMA blend exhibited a bilayer phase separation with the insulator as the bottom layer. This film morphology was attributed to the adhesion of PMMA to the hydrophilic SiO₂ substrate. The blend with P α MS consisted of a trilayer structure with the insulator polymer as the middle layer between the bottom and top semiconductor ones. This film structure was an entropy-driven effect since the separation of the high M_w polymer from the bottom layer would result in energetically unfavorable loss of entropy due to the proximity of the impenetrable rigid substrate. The trilayer films showed the highest mobility of $10^{-1} \text{ cm}^2 \text{ V}^{-1} \text{ s}^{-1}$ exceeding the value of $10^{-2} \text{ cm}^2 \text{ V}^{-1} \text{ s}^{-1}$ for pure diF-TES-ADT (Figure 4a). The improvement in charge carrier transport was related to the favorable morphology of the semiconductor in the phase separated film containing a larger amount of 001 oriented and few 111 crystals. The pristine semiconductor possessed a poor mobility owing to the presence of two different crystal orientations (Figure 4b). On the other hand, blends with PMMA and sPS demonstrated a weaker charge carrier transport than pure diF-TES-ADT films (Figure 4a). Blends with sPS did not phase separate sufficiently to form continuous semiconducting percolation pathways (Figure 4b). In the case of PMMA, a rough

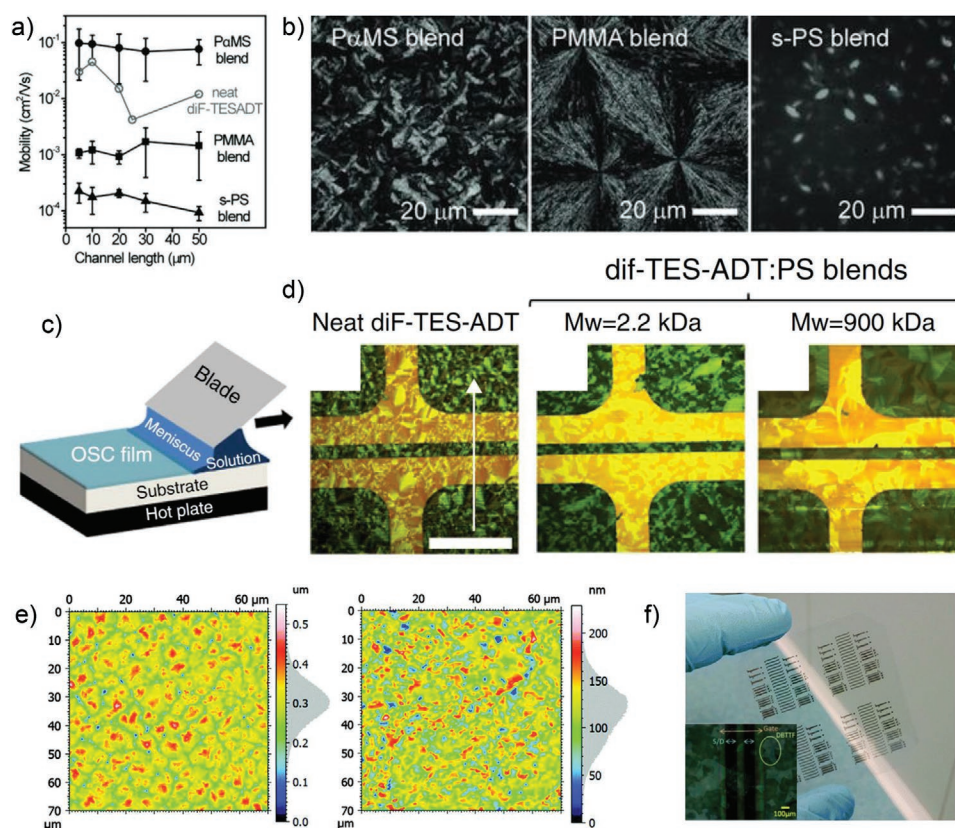


Figure 4. a) Charge carrier mobilities of pristine diF-TES-ADT and within insulator blends for different channel lengths, b) POM images of diF-TES-ADT blend films with different insulator polymers. Reproduced with permission.^[64] Copyright 2012, Wiley-VCH. c) Illustration of blade coating, d) POM images of neat diF-TES-ADT and its blends with low- M_w and high- M_w PS (arrow indicates the direction of blade coating, scale bar 250 μm). Reproduced with permission.^[69] Copyright 2015, Springer Nature. e) AFM height images of PVDF layer (left) and DB-TTF/PS film (right), f) flexible substrate with DB-TTF/PS-based OFET (inset: POM of crystallized DB-TTF/PS in the transistor channel). Reproduced with permission.^[71] Copyright 2015, The Royal Society of Chemistry.

interface between semiconductor and polymer phase was formed. Another essential aspect for the charge carrier transport is processing of the blend film. Blade coating, as illustrated in Figure 4c, is a powerful method to control the morphology and boost the device performance of neat organic semiconductors and their blends. Blade-coated films of diF–TES–ADT blended with an amorphous insulating polymer (PS or P α MS) revealed pronounced charge carrier mobilities of 4.5 cm² V⁻¹ s⁻¹ with low threshold voltage of 1 V and subthreshold swing of 0.5 V dec⁻¹.^[69] While neat diF–TES–ADT films formed crystalline structures with cracks and extended domain boundaries reducing the charge transport, the blends comprised a connected, smooth, and defect-free morphology (Figure 4d). It was also found that M_w of the insulating polymer influenced the phase separation and device performance. At high M_w , fewer domain boundaries appeared and a more effective vertically phase separated bilayer was formed increasing the long-range lateral crystallization diF–TES–ADT (Figure 4d).

In bilayer structures with a semiconductor top layer, the charge carrier transport is determined by the roughness of the interface between both phases.^[39,70] Incomplete phase separation or disruptions initiated by the Marangoni instability cause interfacial charge trapping and scattering sites which limit the overall OFET performance. The effect of a vertical phase separation with a continuous semiconductor top layer was exploited for the planarization of rough flexible substrates to enhance the charge carrier transport in flexible OFETs which is shown in Figure 4f.^[71] To smoothen the interface to a rough poly(vinylidene fluoride) (PVDF) dielectric, blends of dibenzo–tetrathiafulvalene (DB–TTF) and PS were cast as the active layer on flexible OFETs (Figure 4e). The phase separation between PS and DB–TTF planarized the interface to the bottom PVDF dielectric layer. Additionally, the low permittivity ($\epsilon_r \approx 2$) of PS depolarized the underlying PVDF. The charge carrier mobility of these devices reached 0.2 cm² V⁻¹ s⁻¹ being on identical level of pristine DB–TTF cast on smooth, but rigid substrates. The role of a bottom insulating polymer layer on the charge carrier transport has been also studied for bar-coated blends of n-type perylene diimide (PDIC8CN2) and PS.^[30] The film morphology consisted of a trilayer structure with the semiconductor as the middle layer and led to almost an order of magnitude higher electron mobility (2.3×10^{-2} cm² V⁻¹ s⁻¹) than pristine PDIC8CN2 films (5.5×10^{-3} cm² V⁻¹ s⁻¹). At the same time, the threshold voltage dropped from 9 V to almost 0 V and the subthreshold swing (SS) from 0.9 to 0.15 V dec⁻¹. The n-type semiconductors are especially sensitive to interfacial charge trapping by silanol groups at the SiO₂ dielectric of rigid silicon substrates. The decrease of V_{th} and SS for the PS/PDIC8CN2/PS trilayer in comparison to plain PDIC8CN2 was an efficient way to cover the silanol groups at the SiO₂ surface and to lessen the interfacial trapping. The reduced SS was ascribed to a narrower density of states with smaller amount of lower energy sites extending into the band gap.

The charge carrier transport strongly depends on the lattice packing and π -orbital overlap between neighboring conjugated molecules.^[72] Due to weak non-covalent interactions, some small molecular systems, such as pentacene or TBTT, form different crystalline phases that significantly vary in their charge carrier mobilities.^[73,74] Polymorphism of small molecules is also governed by the type of insulating polymer in the blend. Rubrene

crystallized in blends with poly(4-vinylpyridine) (P4VP) and PS in spherulitic domains in an orthorhombic structure and was more disordered in a triclinic phase in PMMA blends.^[75] The higher degree of vertical phase separation in PS and P4VP films was critical for the polymorphism with improved field-effect mobility. Besides the type of insulating polymer, the processing conditions also influence the polymorphism. The film morphology and crystal structure of dibenzotetrathiafulvalene (DB–TTF) in PS blends was controlled by substrate temperature, coating speed, and composition ratio during solution shearing.^[76] For films with major PS content, DB–TTF created a pure γ polymorph with homogeneous isotropic plate-like crystalline domains. A mixed crystal phase of α and γ polymorphs and reduced charge carrier mobility was found for films with DB–TTF as the main component. The difference in uniformity was related to thermodynamic and kinetic processes during vertical phase separation and crystallization. Many polymorphs of high mobility are only metastable and a long-term stability can be achieved in polymer blends. The 2,7-dioctyloxy[1]benzothieno[3,2-b]benzothiophene (C8O–BTBT–OC8) revealed in solution sheared PS blends greater device performance and significantly longer stability of the surface-induced herringbone structure than the neat semiconductor films.^[77] In situ phonon Raman microscopy proved a slow structural transition of C8O–BTBT–OC8 into the unfavorable bulk cofacial phase of poor electrical performance. The stability time of the herringbone structure in blend films depended also on M_w of PS. High M_w ensured a long stability period due to an enhanced continuity of the PS-rich bottom layer in the vertically phase separated films.

3.3. Blends with Conjugated Polymers

Blends of insulating and semiconducting polymers have also been studied, in many cases with P3HT as model compound, regarding the influence of the dielectric matrix on film microstructure and charge carrier transport in OFETs. Already 15 years ago, blends of P3HT-PS and P3HT-MEH-PPV were compared.^[78] For these blends, the field-effect mobility gradually declined upon decreasing the P3HT weight fraction. However, the mobility was higher for blends comprising insulating PS than with semiconducting MEH-PPV (Figure 5a). None of the blends exhibited a morphology beneficial for the charge carrier transport (Figure 5b). P3HT:PS blends showed laterally separated domains, while P3HT:MEH-PPV formed a more interconnected morphology in the in-plane direction. This variation in blend morphology was explained by differences between dipole moments of PS ($p \approx 0.1$ D) and MEH-PPV ($p \approx 3.15$ D). The dipole moment of the surrounding is an important factor for the charge carrier transport, since a polar environment broadens the width of the density of states. In such case, the charge carriers require larger activation energies for the hopping transport between neighboring sites. Consequently, this leads to a reduction in hopping rate and finally in charge carrier mobility. This example proves that apart from the film morphology, other factors also impact the transistor performance.

A vivid improvement of the charge carrier transport in P3HT – insulating polymer blends is achieved by aggregation of the semiconductor into elongated nanofibrils in which

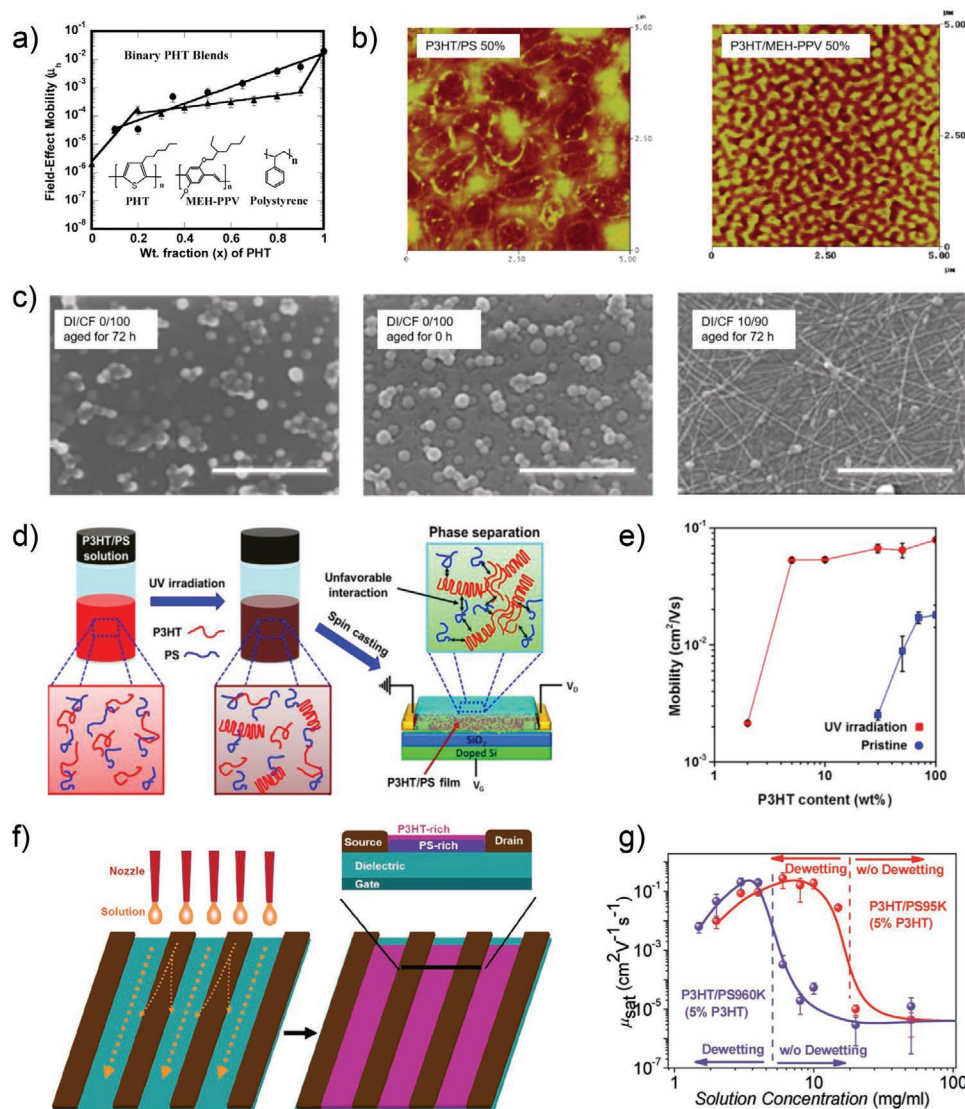


Figure 5. a) Hole mobility of P3HT:MEH-PPV (triangles) and P3HT:PS (circles) blends, b) AFM height images of P3HT:PS (left) and P3HT:MEH-PPV (right) films. Reproduced with permission.^[78] Copyright 2004, American Chemical Society. c) SEM images of P3HT:PS blends dissolved in dioxane/chloroform solution mixtures (scalebar is 1 μm). Reproduced with permission.^[80] Copyright 2009, American Chemical Society. d) Scheme of aggregation in P3HT:PS blend solution and in OFET, e) charge carrier mobility of P3HT:PS blends as a function of P3HT weight ratio. Reproduced with permission.^[81] Copyright 2015, American Chemical Society. f) Schematic illustration of the printing process with the subsequent dewetting and phase separation of the P3HT/PS blend in OFETs. The deposited solution of the blend dewets from the source/drain electrodes and vertically phase separates in the OFET channel. g) Correlation between charge carrier mobility and solution concentration of the P3HT/PS blend at ratio of 5/95 for low- and high- M_w PS. Reproduced with permission.^[83] Copyright 2017, Wiley-VCH.

the conjugated polymer segments are face-to-face stacked. Casting from 1,2-dichlorobenzene solution P3BT assembles in nanowires within a PS matrix. However, such structures were not observed for P3HT because of its higher solubility in the used solvent.^[79] But, deposition of P3HT and PS together from a mixture of chloroform and dioxane yielded working transistors based on composites with only 1% P3HT nanofibrils in the insulating matrix.^[80] Chloroform is a good solvent for both the semiconductor and insulator, while dioxane is a good solvent for PS, but inferior for P3HT. The role of the poor solvent was to induce aggregation of the semiconductor in solution prior to film casting. Fresh and aggregated chloroform solution without

dioxane triggered a morphology of separated P3HT islands in the PS matrix. After addition of dioxane and aging the mixed solution, the P3HT islands became interconnected via elongated nanostructures. This morphology was favored by a higher dioxane concentration and longer aging time (Figure 5c). The phase separated semiconducting nanofibrils embedded in the insulating PS matrix exposed a charge carrier mobility of $10^{-2} \text{ cm}^2 \text{ V}^{-1} \text{ s}^{-1}$ even for P3HT fractions of only 1%.

The introduction of a poor solvent and aggregation time of several hours can be perceived as a rather complicated and long preparation procedure. Recently, UV-irradiation was reported as a more rapid way to form nanofibers of P3HT in chloro-

form dissolved together with PS (Figure 5d).^[81] A mobility of $5 \times 10^{-2} \text{ cm}^2 \text{ V}^{-1} \text{ s}^{-1}$ was achieved for OFETs at P3HT weight fractions of 5% (Figure 5e). Non-irradiated solutions did not show any nanofibrillar aggregates resulting in a mobility of only $10^{-2} \text{ cm}^2 \text{ V}^{-1} \text{ s}^{-1}$ which abruptly dropped upon lowering the P3HT content below 80%. The mobility decrease for minor semiconductor fractions was attributed to isolated P3HT islands in the blend film.

The charge carrier transport in P3HT blends can be further enhanced by initiating a vertical separation between the components as proven for blends of P3HT and PMMA.^[70] Due to the surface energy of the substrate, the more hydrophobic P3HT phase separated to the air interface as continuous layer in the blend film. The phase separation was intensified by extending the drying time of the solution coated film by using a high boiling point solvent. Surprisingly, for blends with more than 5% of the semiconductor, the drain current of the OFETs and P3HT weight content followed an inversely proportional relation. The charge carrier mobility of films with 20% P3HT was \approx three times lower than with 5%. This difference in transistor performance was attributed to variations in surface roughness of the underlying PMMA layer. At higher PMMA fractions, the interface between semiconductor and insulator was more planar, stimulating better ordered P3HT structures favorable for the charge transport. Another recent work reported that the vertical phase separation in P3HT/PMMA bilayers is determined by an interplay of thermodynamic and kinetic factors.^[82] At fastest spin-coating rates, immiscibility and surface energy of the polymers in the blend were responsible for the film morphology, while at slow casting, additional entropic driving forces and solubility limits of the polymers were competing with the other factors, lowering the control over the vertical phase separation.

A vertical phase separation was also induced in printed P3HT/PS bilayer blends by selective dewetting of the deposited solution.^[83] Ink-jet printing is especially attractive as an up-scalable technique for future practical applications.^[84] The deposited solution was confined in the channel region of a tilted OFET substrate because of its dewetting of the metal electrodes and wetting of the SiO_2 dielectric (Figure 5f). The substrate tilting ensured formation of a uniform bilayer film with a short nanofiber-like P3HT morphology during solution flow away from the channel. During solvent evaporation, the top surface of the source and drain electrodes remained free of the polymers and the vertical phase separation between P3HT and PS occurred only in the OFET channel so that the active semiconductor layer covered the complete channel area and connected the electrodes. The location of the active film only in the channel is attractive to avoid parasitic leakage and crosstalk between neighboring transistors in a circuit logic.^[85] The dewetting process of the P3HT/PS solution depended on solution concentration and M_w of PS that both influenced the solution viscosity and finally, the film morphology as well as device performance (Figure 5g). At optimized conditions, an effective field-effect mobility of $1 \text{ cm}^2 \text{ V}^{-1} \text{ s}^{-1}$ with an on/off ratio of 10^7 was found for blends with only 2–5% P3HT content.

As other types of conjugated polymers with superior performance in comparison to P3HT had been developed over the last years, the research focus turned to blends with these systems. For example, blends of organometallic polytellurophenes carrying

different alkyl side chains and high-density polyethylene (HDPE) were applied as active films in OFETs.^[86] Due to the presence of metallic tellurium in the backbone, polytellurophenes provide higher imaging contrast between the semiconducting and insulating phases in the blend. Polytellurophene with linear side chains did not exhibit any change in charge carrier mobility when blended with HDPE at a semiconductor:insulator ratio of 60:40. The blend morphology consisted of spheroidal structures of the insulator polymer with imbedded semiconductor nanofibers (Figure 6a). The fibrillar structures of the semiconductor located between the spheroids ensured percolation pathways for the charge carrier transport. The miscibility between polytellurophene with branched alkyl side chains and HDPE decreased favoring the phase separation and yielding larger domain sizes and thus, higher charge carrier mobility.

Conjugated polymers containing electron accepting and withdrawing segments in the main chain reveal a particularly pronounced device performance,^[87] especially if a fibrillar morphology for efficient charge transporting pathways in binary blends is formed. Polydiketopyrrolopyrrole-dithienylthieno[3,2-b]thiophene (DPP–DTT) of low M_w was blended with PS to favor the self-assembly of the conjugated polymer.^[88] After annealing the blend film above T_g of PS, an interpenetrating, nanowire DPP–DTT network was observed for blends with 60% PS (Figure 6b). The improved DPP–DTT ordering was related to cooperative shifting motion of PS chain segments that supported the movement of DPP–DTT chains homogeneously throughout the film bulk. Due to the fiber interpenetrating network of highly ordered polymer chains together with a predominantly single α -polymorph phase, the charge carrier mobility rose from $1.5 \text{ cm}^2 \text{ V}^{-1} \text{ s}^{-1}$ for neat DPP–DTT to $8.25 \text{ cm}^2 \text{ V}^{-1} \text{ s}^{-1}$ for the blend (Figure 6c). Above 60% PS loading, the mobility declined because of the dilution effect, disrupting the interconnectivity of the nanowire network. For higher M_w of PS, the fibrous network turned gradually into isolated islands reducing the device performance. Identical observations were reported for poly(diketopyrrolopyrrole-terthiophene) (PDPP3T) mixed also with PS and compared to blends with poly-[[N,N-bis(2-octyldodecyl)-naphthalene-1,4,5,8-bis-(dicarboximide)-2,6-diyl]-alt-5,5'-(2,2'-bithiophene)] (P-(NDI2OD-T2)), emphasizing the importance of the fiber morphology for the charge carrier transport through the blend films.^[89] The miscibility between conjugated and insulating polymers was determined by differential scanning calorimetry. Melting temperature of PDPP3T remained unchanged after blending with PS. In the case of P-NDI2OD-T2, its melting temperature decreased in the blend with PS. This observation indicates higher miscibility of P-NDI2OD-T2 in PS, in comparison to miscibility of PDPP3T in the same insulator. The difference in miscibility was also evident in the polymer aggregation in wet films and in the solid blend morphology. In situ UV–vis absorbance indicated stronger aggregation of PDPP3T, inducing an extended and interconnected fiber network in the PS matrix in comparison to the neat conjugated polymer. At elevated PS ratio, the charge carrier mobility increased to $1.5 \text{ cm}^2 \text{ V}^{-1} \text{ s}^{-1}$ owing to high polymer order and a preserved interconnected fiber network. In contrast, for the more miscible (P-(NDI2OD-T2)) the fiber morphology and mobility remained unchanged in the blend (Figure 6d).

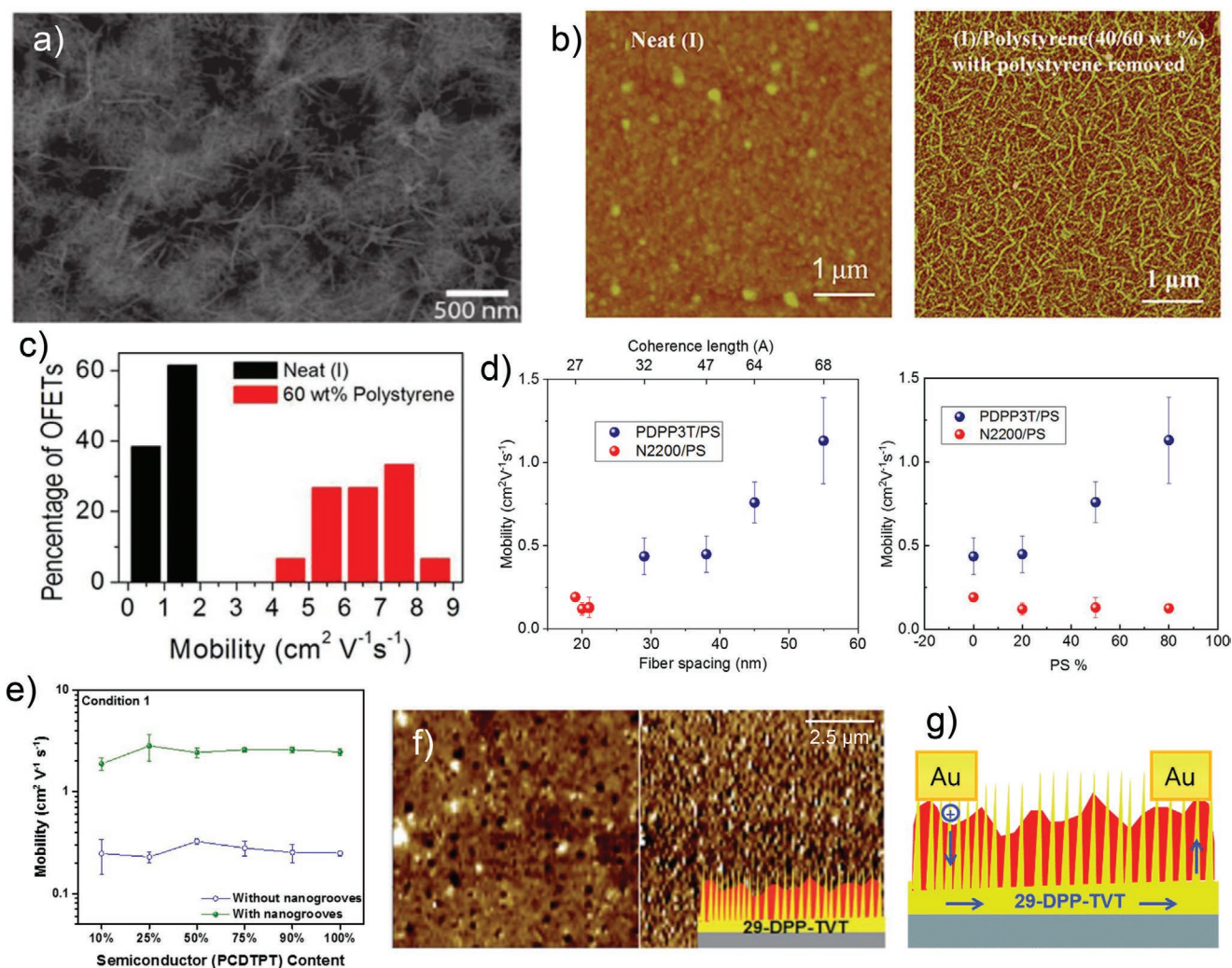


Figure 6. a) Dark-field TEM image of P3HT:HDPE blend. Reproduced with permission.^[86] Copyright 2015, The Royal Society of Chemistry. b) AFM images of neat DPP–DTT with a grainy domain morphology and its DPP–DTT/PS blend (40/60 wt%) showing well-defined fiber network after removal of PS. c) Charge carrier mobility for neat DPP–DTT and the DPP–DTT/PS blend (40/60 wt%). Reproduced with permission.^[88] Copyright 2016, Springer Nature. d) Correlation between charge carrier mobility, fiber spacing, and coherence length of PDPP3T/PS and N2200/PS blends (left) and charge carrier mobility of PDPP3T/PS and N2200/PS blends as a function of PS content (right). Reproduced with permission.^[89] Copyright 2020, American Chemical Society. e) Charge carrier mobility of PCDTPT:PS blends as a function of PCDTPT content. Reproduced with permission.^[90] Copyright 2016, American Chemical Society. f) AFM height (left) and phase (right) images of 29-DPP–TVT:PMMA blend and g) scheme of the charge carrier transport in top-contact OFETs based on 29-DPP–TVT:PMMA blends. Reproduced with permission.^[93] Copyright 2017, The Royal Society of Chemistry.

The unidirectional alignment of the fiber structures further enhances the charge carrier mobility of the polymer blends in OFETs. Mixtures of poly[4-(4,4-dihexadecyl-4H-cyclopenta[1,2-b:5,4-b']dithiophen-2yl)-alt-[1,2,5]thiadiazolo[3,4-c]pyridine] (PCDTPT) and PS were deposited by blade-coating.^[90] At optimized processing conditions, the field-effect mobilities of the films were independent of the blend ratio down to 10% of PCDTPT and were on an identical level as for the neat conjugated polymer (Figure 6e). These values increased by one order of magnitude to $2 \text{ cm}^2 \text{V}^{-1} \text{s}^{-1}$ when the blend was blade-coated on nanogrooved substrates through further promotion of the chain alignment of PCDTPT.^[91] The aligned and interconnected fibers for blend films with 10 wt% PCDTPT resulted in an anisotropic transport with higher mobilities along the orientation direction. It was concluded that

PCDTPT phase separated and interacted more strongly with the surface relative to PS. Recent studies suggested a better short-range ordering of PCDTPT when it was diluted in blends with an amorphous polymer such as PS and PMMA.^[92]

Phase separated semiconductor/insulator blend films with a semiconductor bottom layer are unsuitable for top contact OFETs. This limitation has been overcome for blends of poly[2,5-bis(2-decyltetradecyl)pyrrolo[3,4-c]pyrrole-1,4-(2H,5H)-dione-(E)-1,2-di(2,20-bithiophen-5-yl)ethene] (29-DPP–TVT) and PMMA.^[93] During spin-coating of the 29-DPP–TVT–PMMA mixture from chlorobenzene, the semiconductor solidified first as the bottom layer and penetrated into the upper insulating layer due to the Marangoni instability as illustrated in Figure 6f,g. Without this instability, the 29-DPP–TVT bottom layer would be separated from the

source and drain top electrodes by insulating PMMA hindering charge injection into the semiconductor. The interpenetrating “spike”-like morphology of 29-DPP–TVT through the insulating top layer ensured an interconnection to the top electrodes (Figure 6g). The elevated crystallinity of 29-DPP–TVT was preserved in the blend film leading to a charge carrier mobility of $0.7 \text{ cm}^2 \text{ V}^{-1} \text{ s}^{-1}$.

An irregular phase separation between the insulating and conjugated polymers might be related to the polydispersion of the semiconductor. Spin-coated blends of PCDTPT:PS at weight ratio of 5:95 phase separated along a distribution gradient of the semiconductor in the insulator matrix.^[94] Absorption analysis of plasma etched films demonstrated that the blend morphology comprised a well-ordered high- M_w PCDTPT top layer and isolated less crystalline low- M_w PCDTPT islands embedded in the bulk PS matrix (Figure 7a). Due to their poor solubility in PS and lower surface free energy, the better ordered PCDTPT chains phase separated as the top layer, while the less ordered fraction with higher solubility remained in the PS matrix (Figure 7a). Additionally, PS concentrated at the substrate interface driven by its higher surface free energy. The well-ordered PCDTPT top phase ensured a field-effect mobility of $0.5 \text{ cm}^2 \text{ V}^{-1} \text{ s}^{-1}$. High negative gate-bias stresses applied to the transistor provoked a large irreversible shift of the threshold voltage to negative voltages as holes were injected from the top semiconductor layer into the PCDTPT islands embedded in the PS matrix. This device behavior was considered for write-once, read-many-times memory. To realize reversible shifts of the transfer curves for flash-type memories, an additional 4.0 nm thin top n-type N,N' -dioctyl-3,4,9,10-perylene diimide (C8-PDI)

layer was deposited to inject electrons for neutralization of the trapped holes in the embedded PCDTPT islands (Figure 7a,b).

The approach of a semiconductor/insulator blend as a charge storage electret was expanded to photonic transistor memories. The devices consisted of a blend electret based on poly(9,9-dioctylfluorenyl-2,7-diyl) (PF) and PS or PMMA with a top semiconducting pentacene layer (Figure 7c).^[95] The threshold voltage was reversibly shifted to positive values by applying a positive gate voltage through the electron injection from the semiconductor layer into the dielectric blend layer, while after a negative gate voltage, the transfer curves returned to their initial positions. The devices with the PS-based blend revealed a stronger shift of the threshold voltage and therefore, a larger memory window than with PMMA. This behavior was attributed to a more efficient electron capture of the aromatic ring in PS and its greater electron-storing ability. The shift in threshold voltage was further increased by additional light illumination during gate voltage since the PS matrix captured more photogenerated electrons from PF. The illuminated PF/PS devices raised the I_{ds} current from $5.5 \times 10^{-11} \text{ A}$ to $3.2 \times 10^{-5} \text{ A}$ and operated under reversible cycle stability during photon-writing, reading, and electrical-erasing (Figure 7d). The memory window decreased with lowered PF concentration in the PS matrix, especially below 50% PF. Additionally, the charge transfer efficiency between the semiconductor and memory layer was intensified by an improved interfacial contact area which was achieved by a suitable processing solvent.

Removable low M_w insulators are an alternative strategy for blends with organic semiconductors. Poly-diketopyrrolopyrrole-co-thienovinylthiophene (DPP–TVT) was mixed with a

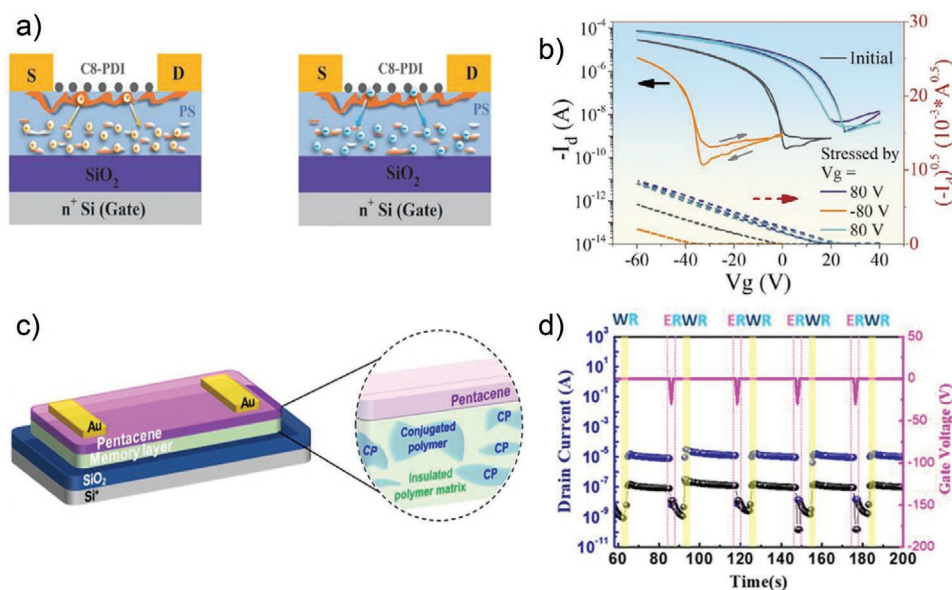


Figure 7. a) Schematic illustration of the device structure with injection of holes or electronics into the PCDTPT–PS blend films where the charges are trapped in the poorly ordered PCDTPT islands. The top layer consists of highly ordered PCDTPT phase serving as the charge transport layer. This aggregation gradient is formed spontaneously during spin-coating. The subsequently sublimated C8-PDI layer ensures an injection of electrons to neutralize the trapped holes. b) Reversible shift of the transfer curves ($V_d = -60 \text{ V}$) of the PCDTPT–PS 5:95 blend OFET containing the 4 nm of C8-PDI top layer. The shift is triggered by applying a gate-bias stress of 80 V or -80 V . Reproduced with permission.^[94] Copyright 2020, Wiley-VCH. c) Device structure of the photonic transistor memory using the PF/PS blend with a top pentacene layer, d) photowriting (at 405 nm; 10 mW cm^{-2} and 0.55 mW cm^{-2} for 1 s) and erasing cycles of the transistor memory based on PF/PS (1:1). Reproduced with permission.^[95] Copyright 2019, American Chemical Society.

low-boiling-point branched polyethylene.^[96] The additive promoted aggregation and phase separation of DPP–TVT but reduced its crystallinity. Owing to its boiling point of only 135 °C, polyethylene was removed by annealing at elevated temperatures without affecting the morphology and charge carrier transport of the conjugated polymer in a wide blend ratio.

While thermoplastic polymers such as PMMA and PS are suitable for bending applications of the blend OFETs because of their Young's modulus, elastomers are required for stretchable devices to withstand the higher strain. In stretchable applications, polymer aggregation and nanofiber formation are required to ensure the charge carrier transport at large strain. It was reported that the aggregation and molecular ordering of a high M_w diketopyrrolopyrrole (DPP)-based polymer were enhanced in the blend with polystyrene-block-poly(ethylene-co-butylene)-block-polystyrene (SEBS).^[97] The resulting fibrillar network of the conjugated polymer vertically phase separated at the bottom and top interfaces of the blend film. Through more planarization of the polymer backbone, stronger aggregation and predominant edge-on arrangement of the DPP polymer, charge carrier mobility of the blend films, containing 30 wt% of the semiconducting polymer, increased from 0.3 cm² V⁻¹ s⁻¹ for the neat polymer to 1.5 cm² V⁻¹ s⁻¹.

As discussed in this section, OFETs based on either small molecules or conjugated polymers benefit from blending with an insulating polymer. The microstructure of the semiconductor fraction in the blend is tailored by the type of insulating polymer and casting conditions. Vertically phase separated bi- and tri-layer structures promote the morphology formation and charge carrier transport of the semiconductor. The transport is especially favored when a molecular long-range alignment is initiated in the blend. Moreover, utilization of an insulating polymer can lower interfacial charge trapping on rough or polar substrates. For conjugated polymers, presence of an insulating polymer in the blend can trigger formation of elongated nanofibrils, that significantly contribute to high charge carrier mobilities by interconnection of semiconducting domains in the lateral direction of the film.

4. Environmental Stability

One of the main drawbacks of organic semiconductors, in comparison to inorganic counterparts, is their poor environmental stability, which greatly reduces the lifetime of electronic devices.^[98,99] Especially n-type semiconductors are sensitive to degradation due to atmospheric oxygen and moisture.^[100] A drop in charge carrier mobility is typically observed even during few hours of storage of the OFETs in ambient conditions. P-type semiconductors are also affected by oxygen or moisture.^[101,102] For example, P3HT-based OFETs exhibit an immediate rise in off-current caused by oxygen doping diminishing the on/off ratio to small values.^[103] To promote the stability of the devices, barrier layers are deposited on the top of the charge transporting films. However, solution casting of the encapsulation material can dissolve the underlying semiconducting layer.^[70,104] Vacuum deposition of encapsulating layers, by, for example,

chemical vapor deposition, circumvents such problems, but significantly increases the complexity of the device fabrication.^[105,106] Blending the organic semiconductor with an insulator polymer in solution is an efficient way to achieve an encapsulation layer through spontaneous phase separation. The semiconductor can be encapsulated in one solution coating step if a vertical phase separation occurs with the dielectric material as the upper layer of the bilayer film.

Since OFETs with P3HT rapidly degrade upon exposure to air, this polymer has been commonly used for studies on device stability. It was proven that blending P3HT with HDPE initiates bilayer structures with semi-crystalline HDPE composing the upper encapsulating layer. The bilayer structures were fabricated by controlled crystallization sequence of the semiconducting and insulating polymers. OFETs with such P3HT/HDPE bilayers did not show any doping effects in air thanks to encapsulation of the bottom semiconducting layer.^[42] A similar bilayer morphology was achieved for P3HT and amorphous PS blends, where the bottom semiconducting layer comprised P3HT fibrils. OFETs consisting of these bilayers maintained their performance with pronounced on/off ratio for 7 days, while at the same conditions, the off-current for devices with pristine P3HT films increased by almost two orders of magnitude as result of doping (Figure 8a).^[81] Another work reported that high M_w paraffin in comparison to PDMS can further improve the environmental stability of P3HT.^[107] The conjugated polymer was aggregated by UV irradiation of the blend solution to induce fiber structures and to promote in this way, the charge carrier mobility in the spin-coated films. While the mobility of neat fibrous P3HT significantly declined from 0.095 to 0.031 cm² V⁻¹ s⁻¹ during 4 weeks at ambient environment, the value remained constant at 0.072 cm² V⁻¹ s⁻¹ for the paraffin blend (Figure 8b). The device stability with blends of PS or PDMS revealed a stronger decrease in the same study. All blend films contained a similar morphology of a vertical gradient of the phase separated P3HT fibers (Figure 8b). The semiconducting region was preferably distributed near the bottom surface of the blend films through precipitation of the P3HT fibers during spin coating. The top paraffin matrix formed a tight top barrier layer against moisture in ambient air ensuring the stability of the device.

Environmental stability of OFETs has also been thoroughly studied for conjugated small molecules–insulator blends. Perylene diimide (PDI) derivatives are commonly used as electron transporting semiconductors thanks to their good charge carrier transport and ability to self-assemble in highly crystalline structures.^[108,109] However, OFETs based on PDIs typically suffer from poor environmental stability under operation leading to a significant shift of the threshold voltage to positive values, which was investigated by bias-stress measurements.^[30] This shift is initiated by charge carrier trapping related to oxidation products or moisture. A trilayer film of PS/PDI8CN2/PS was coated by bar assisted meniscus shearing.^[30] The two PS layers prevented trapping at the interface with the SiO₂ dielectric and diffusion of oxygen molecules into the semiconductor layer from air. An OFET stability for 150 days was achieved in comparison to the pristine PDI8CN2 film, for which the device degraded

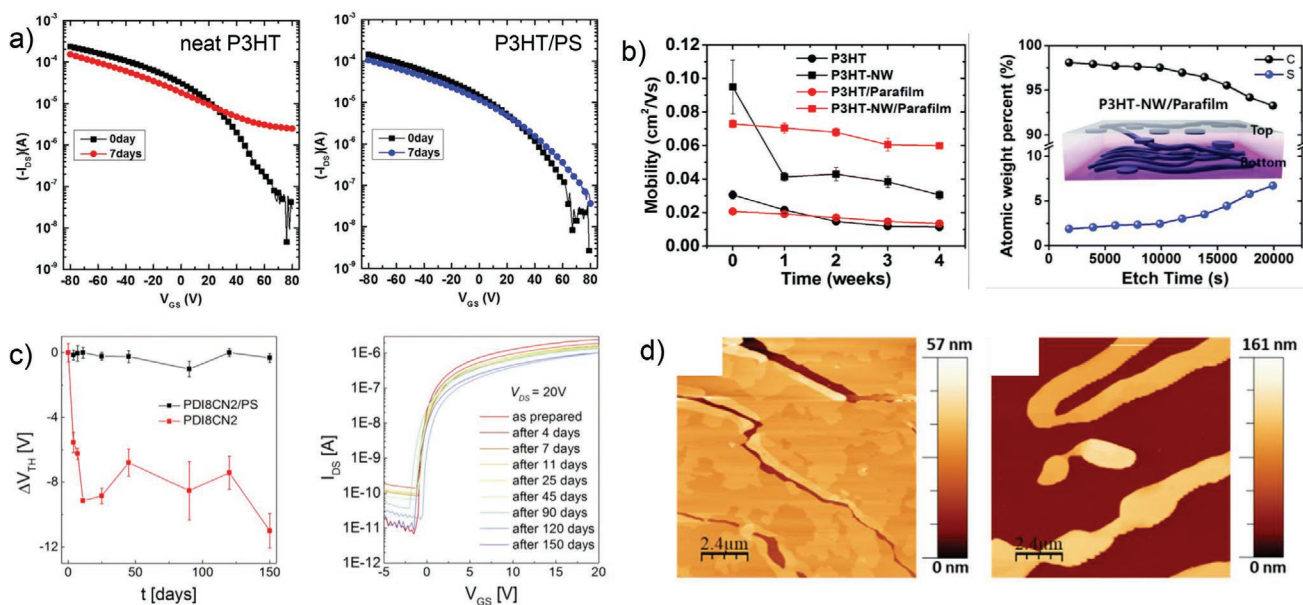


Figure 8. a) Transfer curves of P3HT and P3HT/PS blends measured prior and after exposing the devices to air for seven days. Reproduced with permission.^[83] Copyright 2015, American Chemical Society. b) Charge carrier mobility of spin-coated neat and paraffin blended P3HT with and without nanowire (NW) morphology as a function of exposure time to ambient air (left) and XPS depth profiles of spin-coated nanowire P3HT/paraffin blend films and illustration of the blend morphology of a vertical gradient distribution of P3HT (right). Reproduced with permission.^[107] Copyright 2019, Royal Society of Chemistry. c) Threshold voltage of OFETs with PDI8CN2 and PDI8CN2/PS blends as function of air exposure (left) and transfer characteristics of PDI8CN2/PS blends measured after specified period of exposure (right). Reproduced with permission.^[30] Copyright 2018, American Chemical Society. d) AFM height images of C8-BTBT films before (left) and after (right) morphology degradation. Reproduced with permission.^[34] Copyright 2018, American Chemical Society.

within few hours (Figure 8c). Similar improvement in OFET stability was observed for spray-coated blends of TIPS-pentacene with PMMA or PS.^[62] The film was deposited onto a SiO₂ dielectric and also comprised a vertically separated structure with the semiconductor located in the intermediate region between both insulating layers. The blend films did not reveal any significant shift of the threshold voltage even after 13-month storage in ambient conditions. Film stability can also concern morphology changes over time as observed for C8-BTBT (Figure 8d).^[34] Bar-coated continuous films deposited on Si/SiO₂ substrates turned into separated islands after 4 months. These structural changes are unfavorable for the charge carrier transport in transistors and were related to gradual dewetting. To overcome morphological instabilities, PS/C8-BTBT/PS trilayers were bar-coated. The insulating upper layer was only 1 nm thin. Bottom and top encapsulation of the C8-BTBT layer restrained the dewetting process due to the hydrophobicity of the underlying insulating layer.

Blending organic semiconductors with insulating polymers in combination with suitable processing conditions yields vertically phase separated film morphologies that refine the OFET stability. By prevention of oxygen and moisture diffusion into the semiconductor layer, the charge carrier mobility and on/off ratio become stable over long time periods. The phase separated bottom insulating layer reduces interfacial charge trapping and contributes to better device stability during long-term operation by minimizing bias stress. Finally, the higher viscosity and adhesion of semiconductor/insulator blend films prevents a morphology degradation which can occur for pristine semiconducting films over a prolonged storage.

5. Semiconductor–Insulator Blends for Elastic OFETs

As a main advantage, organic semiconductors show smaller tensile modulus than their inorganic, rigid counterparts like silicon, and bear therefore, great potentials for flexible or stretchable electronics.^[25,110] As mentioned in the introduction, flexible electronics can be implemented in a broad range of applications reaching from medical to smart clothing and internet of things.^[111,112] However, despite lower tensile modulus, organic semiconductors still require further development to achieve sufficiently high elasticity for stable charge carrier transport under severe external stresses. For this reason, new organic semiconductors have been designed to promote their electromechanical behavior.^[113,114] It is proven that semiconducting polymers of high M_w bear greater resilience to cracking as a result of tie chains between ordered domains.^[115–117] This methodology is especially beneficial for increasing the elasticity of films containing small molecular semiconductors that are highly crystalline and brittle.^[118] Conjugated polymers are more suitable for flexible applications because of their higher elasticity, although they also exhibit deterioration of their structure and electrical properties at serious strain. The mechanical properties of semiconducting polymers are enhanced in blends with elastomers or thermoplastic insulators. The smaller tensile modulus of the blends originates from the increase in free volume of the conjugated polymers and lowered T_g .^[16]

Crucial factors determining elasticity of the organic semiconductors are film morphology and crystallinity. Neat P3HT with a disordered microstructure sustained strains above 100% without visible cracking (Figure 9a).^[116] As a drawback of low

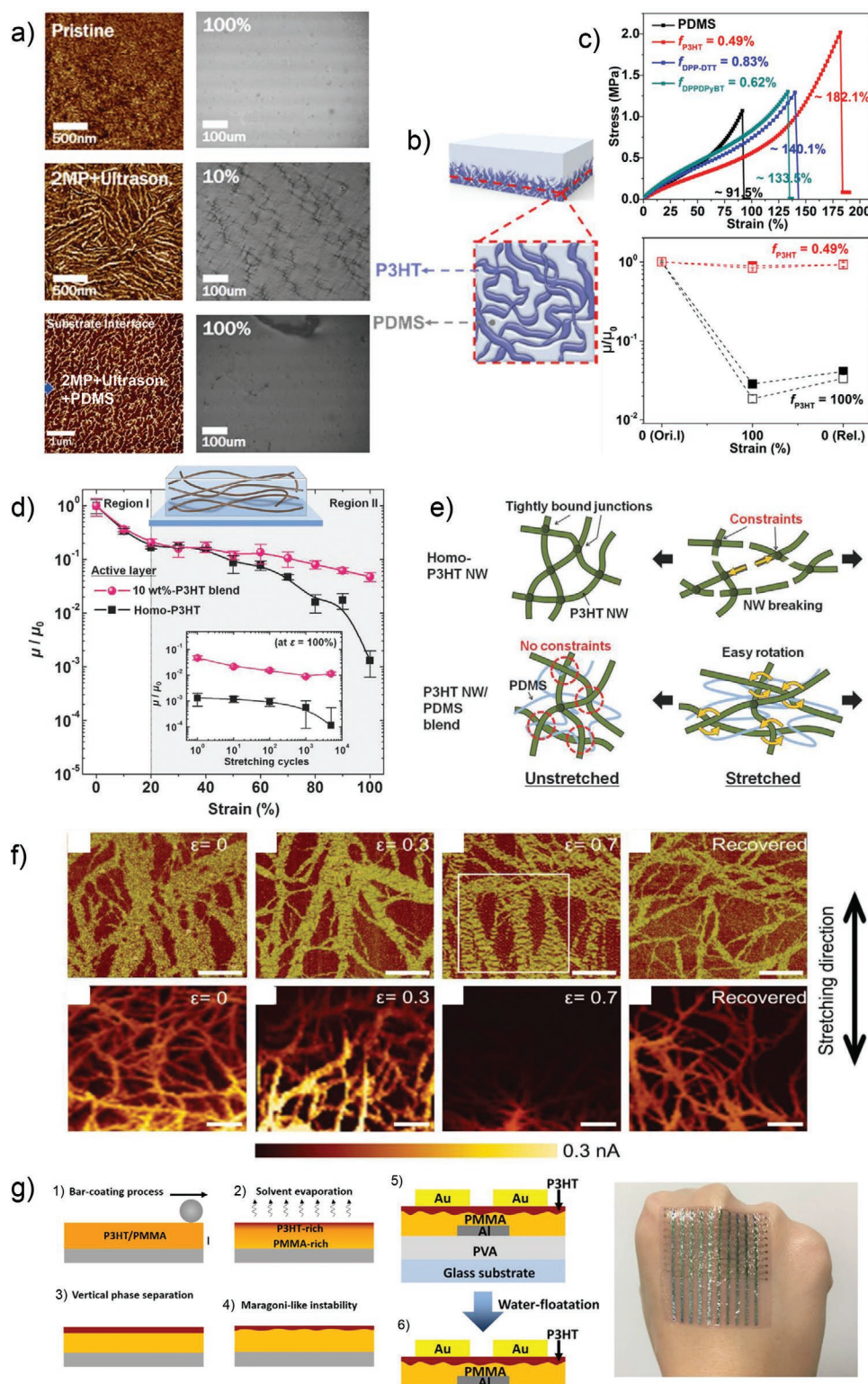


Figure 9. a) AFM of top film surface for pristine (disordered) and 2-methylpentane (2MP) treated and ultrasonicated (aggregated) P3HT as well as of bottom surface of aggregated P3HT/PDMS blend film. Optical microscopy images show corresponding stretched films. Reproduced with permission.^[116] Copyright 2016, American Chemical Society. b) Illustrated interpenetrating polymer network at the interface between vertically phase separated P3HT and PDMS. c) Stress–strain curves of freestanding films of neat PDMS and corresponding blends with conjugated polymers (top) and normalized charge carrier mobility measured parallel (solid) and perpendicular (empty) to the charge transport direction under 100% strain for neat P3HT film (100%, black) and PDMS/P3HT blend (0.49 wt% P3HT, red) (bottom). Reproduced with permission.^[119] Copyright 2017, American Chemical Society. d) Normalized charge carrier mobility as a function of strain for neat P3HT and PDMS:P3HT blend. Bottom inset shows the normalized charge carrier

order, the corresponding OFET mobility of $10^{-3} \text{ cm}^2 \text{ V}^{-1} \text{ s}^{-1}$ was rather poor. The charge carrier transport was improved to $9 \times 10^{-2} \text{ cm}^2 \text{ V}^{-1} \text{ s}^{-1}$ by aggregation of the polymer into highly ordered nanofibrils by ultrasonication. However, the pronounced crystalline and nanofibrillar morphology, presented in Figure 9a, weakened the mechanical flexibility of the P3HT films and generated cracks already at 5% strain. To induce elasticity and to enhance the mechanical properties, small fractions of the conjugated polymer were blended into a PDMS matrix of low tensile modulus. Both components were highly insoluble in each other and the phase separation between the fractions was additionally promoted by the higher inter- and intramolecular order of the conjugated polymer chains in the blend. The strong aggregation and high molecular order of the P3HT chains in the presence of PDMS in solution and thin film was demonstrated by more intense and red-shifted low energy bands in the UV-vis spectra. As described earlier, the blend morphology depends also on the surface energy of the substrate on which the blend film is deposited. On substrates with high surface energy, spin-coated P3HT and PDMS blend films vertically phase separated because the elastomer fraction tended to the air/blend interface, while the nanofibers accumulated at the blend/substrate interface. It was indicated that the PDMS/P3HT interface was composed of a phase-separated interpenetrating polymer network (IPN) due to diffusion of PDMS chains into the P3HT underlying layer in the last stage of coating (Figure 9b). The higher mechanical strength and elasticity of the blend films in comparison to neat PDMS were related to this specific vertically phase separated IPN (Figure 9c).^[119] Additionally, the well-ordered P3HT nanofibers in the bottom layer of the blend film improved the charge carrier mobility to $0.24 \text{ cm}^2 \text{ V}^{-1} \text{ s}^{-1}$ at P3HT fractions below 1%. These blend films sustained a strain of 100% without significant deterioration of either the film structure or charge transport properties (Figure 9a), whereas under these conditions, the device performance of neat P3HT significantly dropped (Figure 9c).^[119] To gain insight into the fracture mechanism of the P3HT fibers under strain, PDMS blend films with a homogenous P3HT distribution were studied. Two regions were identified for the normalized charge carrier mobility as a function of strain for the neat and blended P3HT films (Figure 9d). At the beginning of stretching, for strain between 0% and 20%, the mobility decreased significantly for both devices. In the 2nd region up to 100% strain, the performance of the neat polymer severely degraded, while the operation remained stable for the blend film. The increased elasticity of the P3HT nanofibrils:elastomer blends was attributed to smaller constraints between fibrils in the PDMS matrix (Figure 9e).^[144] Films of neat P3HT nanofibrils contained pronounced fibrillar entanglements as the main origin for breaking during elongation (Figure 9e). In blends with large PDMS fraction, tight junctions of P3HT fibers

restricted a rearrangement in the elongation direction and dissipation of mechanical stress.

Further information on the charge transport mechanism of stretched P3HT nanofibrils was gained for blends with SEBS.^[120] The fibers phase separated to the surface of the rubber matrix and assembled into a network of wide bundles. Conductive AFM displayed that with increasing elongation of the blend, first narrow bundles were disconnected followed by cracking of bundles mainly aligned in the stretching direction, both factors significantly limiting the current flow (Figure 9f). The morphology and electrical conduction were recovered to the initial states when the strain was completely released. Analogous to the current, the hole mobility in OFETs gradually decreased with higher elongation and repeated stretching cycles. It was concluded that the decline in mobility was related to mechanical fatigue of the narrow bundles and crack propagation in the wide ones. In another work, paraffin as an alternative insulator matrix was reported and compared to PDMS for stretchable P3HT fibers.^[107] For neat P3HT fibers and blended in PS, microfractures were generated already at a small strain level of 6%, while they appeared in blends with PDMS at 62% and paraffin at 50% strain.

Other elastic applications of P3HT include bendable OFETs that require thermoplastic insulating polymers. Flexible self-standing active films were fabricated by blending P3HT with a great excess of PMMA to create bilayer structures with an ultrathin semiconductor top layer during bar-coating (Figure 9g).^[121] The P3HT morphology was controlled by concentration of both fractions and blend ratio. In this setup, the bottom PMMA layer was exploited as dielectric in OFETs leading to only negligible gate leakage currents and charge carrier mobility of $0.02 \text{ cm}^2 \text{ V}^{-1} \text{ s}^{-1}$. The devices were stripped from the glass substrates on water and could be attached to curved surfaces proving the flexibility of self-standing films (Figure 9g).

As discussed earlier, the charge carrier mobility in OFETs is significantly enhanced for donor-acceptor polymer nanofibers which are formed in the insulating matrix of a blend. But, the nanofiber self-assembly in the blends is also important for mechanical robustness of the charge transport during applied stress. In contrast to neat 2,5-di-2-thienylthieno[3,2-b]thiophene (DPP2T) that assembled in stacked polymer aggregates with random orientations, at a DPP2T:PS ratio of 15:85, a blend film of a phase-separated nanofiber network of the conjugated polymer in the insulating matrix was grown (Figure 10a).^[122] The charge carrier mobility increased from $0.80 \text{ cm}^2 \text{ V}^{-1} \text{ s}^{-1}$ for neat DPP2T to $3.1 \text{ cm}^2 \text{ V}^{-1} \text{ s}^{-1}$ for the fiber structures. From temperature-dependent FET characteristics, it was concluded that the charge carrier transport along the conjugated polymer backbones was mainly contributing to the superior device performance of the fiber network, whereas randomly oriented aggregates surrounded by amorphous regions in the

mobility as a function of stretching cycles at 100% strain. Top inset illustrates the blend morphology with homogenous distribution of P3HT in the PDMS matrix, e) breaking mechanism of neat P3HT fibrils and blended with PDMS upon stretching. Reproduced with permission.^[144] Copyright 2016, Wiley-VCH. f) Mode phase and conductive mode AFM images of P3HT/SEBS blend films at different strains under uniaxial stretching (scale bars are 500 nm in phase and 1 μm in conductive images). Reproduced with permission.^[120] Copyright 2015, Wiley-VCH. g) Schematic illustration of the processing steps toward vertically phase separated freestanding P3HT/PMMA films and their implementation in flexible OFETs. Reproduced with permission.^[121] Copyright 2018, American Chemical Society.

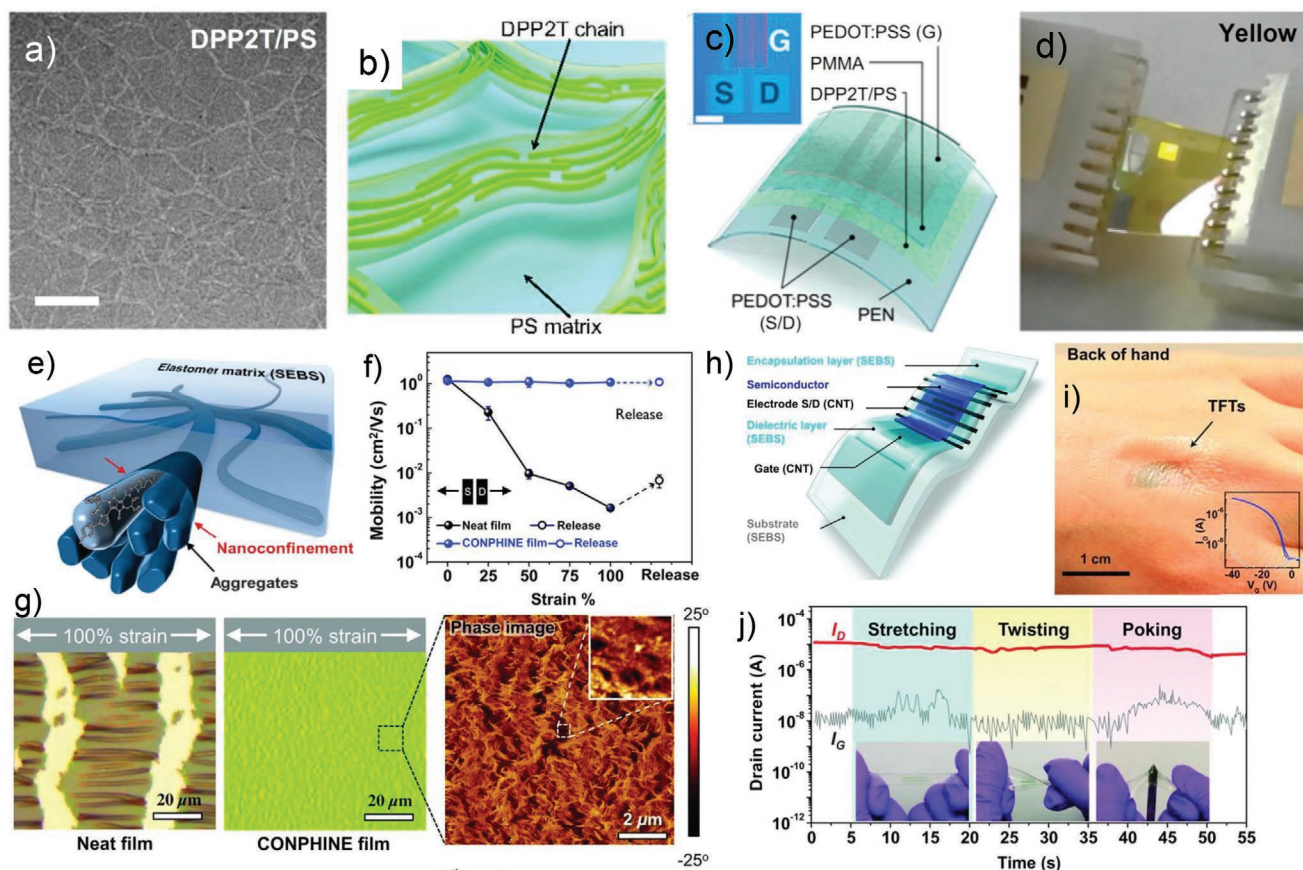


Figure 10. a) TEM image of the DPP2T/PS film (scale bar is 200 nm), schematic illustration of the b) structural morphology in DPP2T/PS films, and c) corresponding flexible OFETs (inset shows transistor channel with scale bar of 500 μm). d) Image of a yellow PLED with the integrated FET during bending. Reproduced with permission.^[122] Copyright 2015, National Academy of Sciences. e) illustration of DPPT–TT fibrils embedded in the SEBS matrix, f) charge carrier mobility of neat DPPT–TT (black) and DPPT–TT:SEBS blend films (blue) at different strains parallel to the charge transport direction, g) optical microscope images of neat DPPT–TT (black) and DPPT–TT:SEBS blend films at 100% strain as well as AFM phase image of the blend, h) device structure of the fully stretchable transistor based on DPPT–TT:SEBS blend film, i) its application on the back of a hand, and j) drain and gate current of the transistor under different mechanical stressing. Reproduced with permission.^[123] Copyright 2017, American Association for the Advancement of Science.

neat DPP2T film caused a paracrystallinity-dominated π – π transport and limited the conduction (Figure 10b). Flexible and transparent OFETs were constructed based on the active DPP2T:PS blend films solution deposited on poly(ethylene-2,6-naphthalate) substrates and inkjet-printed poly(3,4-ethylene dioxythiophene):poly(styrenesulfonate) (PEDOT:PSS) electrodes (Figure 10c). The charge carrier mobility of $0.80 \text{ cm}^2 \text{ V}^{-1} \text{ s}^{-1}$ remained stable during 1000 bending cycles at a radius of 5 mm. The transistors were integrated as driving element directly on top of flexible polymer light-emitting diodes (PLED) (Figure 10d). The luminance of 252 cd m^{-2} was reached by supplying a gate voltage-modulated drain source current to the bended PLED.

The fiber formation was also the key aspect for the stretchability of high mobility donor–acceptor poly(2,5-bis(2-octyldodecyl)-3,6-di(thiophen-2-yl)diketopyrrolo[3,4-c]pyrrole-1,4-dione-alt-thieno[3,2-b]thiophene (DPPT-TT) in SEBS.^[123] At 30 wt%, DPPT–TT self-assembled into elongated 50 nm thin fibrils mainly in the bottom and top layers in the elastomer matrix favoring in this way, the phase separation (Figure 10e,g). The DPPT–TT polymer chains were aligned

with their long axis along the fibrils (Figure 10e). The lower T_g of the nanofibers (60 °C) in comparison to thick pristine DPPT–TT films (130 °C) suggested a smaller elastic modulus of the nanostructures. The pronounced elasticity of the blend allowed strains up to 100% without damaging the film structure and maintaining a field-effect mobility of $\approx 1 \text{ cm}^2 \text{ V}^{-1} \text{ s}^{-1}$ (Figure 10f,g). In contrast, under the same conditions, the neat DPPT–TT film macroscopically cracked, while the corresponding mobility dropped three orders of magnitude (Figure 10f,g). The blend films were incorporated in fully stretchable transistors containing carbon nanotube networks as the electrodes, SEBS as dielectric layer, stretchable substrate, and encapsulation layer that were applied as e-skins on human epidermis (Figure 10h,i). The drain current of these devices remained stable during serious mechanical stress (Figure 10j).

The recovery of cracks by self-healing is an important concept to improve the reliability of stretchable OFETs. 2,6-pyridinedicarboxamine moieties were introduced in both the semiconducting DPP-TVT and PDMS to induce a metal–ligand coordination complex with Fe(III) ions between the two physically blended polymers and in this way, to facilitate

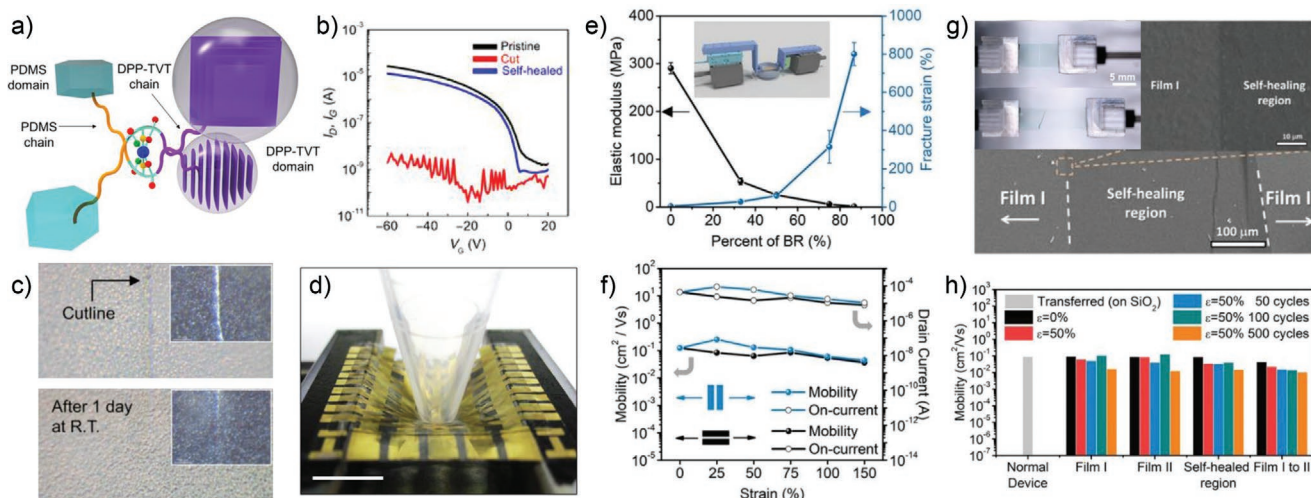


Figure 11. a) Schematic illustration of dynamically cross-linked DPP and PDMS domains through complexation, b) transfer curves of pristine, cut, and self-healed DPP–TVT:PDMS transistors, c) optical microscope images of damaged and self-healed DPP–TVT:PDMS blend films, d) stretched active-matrix DPP–TVT:PDMS transistor array by poking with a plastic bar. Reproduced with permission.^[124] Copyright 2019, American Association for the Advancement of Science. e) Elastic modulus and fracture strain for different blend ratios of DPP–TVT:BR, f) charge carrier mobility and drain current of 1:3 DPP–TVT:BR blend film as a function of elongation, g) SEM image on the self-healed region of the DPP–TVT:BR blend OFET (left inset: film before healing and stretched film after healing), h) charge carrier mobility for self-healed 2:3 DPP–TVT:BR blend films measured for different regions before and after stretching cycles. Reproduced with permission.^[125] Copyright 2020, Wiley-VCH.

dynamic cross-linking (Figure 11a).^[124] The blend film of 1:5 DPP–TVT:PDMS exhibited a charge carrier mobility of $0.1 \text{ cm}^2 \text{ V}^{-1} \text{ s}^{-1}$ and a high elasticity similar to human skin. The blend morphology consisted of phase separated DPP–TVT nanoparticles dispersed in the PDMS matrix. Dichroic and X-ray data indicated that during stretching, the applied strain was mainly absorbed by the elastomer matrix, while preserving the crystalline regions of the semiconducting polymer. The on-currents and mobility of the OFETs were highly sensitive to stretching and significantly decreased by five orders of magnitude at 100% strain of the devices, but almost recovered after releasing the strain. Mechanically introduced scratches in the blend film almost completely disappeared during 1-day self-healing (Figure 11c). Due to the self-healing of the macroscopic defect, the charge carrier mobility was almost completely recovered as evident from the transfer characteristics of the transistor in Figure 11b. To prove applicability of these blend films, a 5×5 stretchable strain-sensitive active-matrix transistor array was fabricated for 3D mapping of surface deformations (Figure 11d). During poking of the sensor array, the on-currents from multiple pixels were recorded resulting in a 3D hemispheric deformation map. In another example, self-healing was achieved in physical blends of DPP–TVT and butyl rubber (BR) as the elastomer matrix.^[125] The blends at ratio of 1:8.5 DPP–TVT:BR revealed a low Young's modulus of only 1 MPa and a high elongation at break of 800% (Figure 11e). These mechanical properties were related to low T_g and a highly entangled network of the BR matrix resisting chain slippage and scission. The charge carrier mobility of the blends remained constant in the range of $0.12\text{--}0.16 \text{ cm}^2 \text{ V}^{-1} \text{ s}^{-1}$ up to a strain of 150% (Figure 11f). The healing was performed during adhesion of two films that could afterward sustain strains of 150% (Figure 11g). The charge carrier mobility for neat films and across the self-healed region was maintained within the

same order of magnitude at 50% strain for multiple cycles (Figure 11h). The self-healing process was again attributed to the segmental motion of low T_g BR chains allowing a reorganization of the DPP–TVT polymer chains to create the necessary conducting pathways at the interface of the two adhered films. With the increase of BR content, the DPP–TVT aggregates turned into a mesh-like network of interpenetrating fibrils uniformly distributed within the BR matrix of the phase separated blend. As in the other cases, this fibril morphology of the conjugated polymer ensured charge transport at high deformation.

Semiconducting small molecules possess a tensile modulus higher than conjugated polymers. Their brittle crystalline structure is therefore less favorable for applications in flexible electronics. Blending with elastic polymers reduces the tensile modulus of the active film and enhances the stress dissipation.^[25] Blends of two semiconducting small molecules, 7,7'-[4,4-bis(2-ethylhexyl)-4H-silolo[3,2-b:4,5-b']dithiophene-2,6-diyl]bis[6-fluoro-4-(5'-hexyl-[2,2'-bithiophen]-5-yl)benzo[c][1,2,5]thiadiazole] (DTS-(FBTTh₂)₂), and [6,6]-phenyl C71 butyric acid methyl ester (PC₇₁BM), were solution coated together with additives of 1,8-dioctane (DIO) and PS.^[118] The blend morphology comprised a phase separated morphology with uniformly distributed domains of PS. The additives enlarged the crack-onset from $\approx 1\%$ to 4% strain, while the tensile modulus of the (DTS-(FBTTh₂)₂):(PC₇₁BM) film declined from 17 to 5 GPa upon addition of DIO and PS. Despite a much smaller elasticity of blends with small molecules than with conjugated polymers, recent studies show a promising trend in development of more stretchable systems containing small molecules.^[126]

Increasing overall elasticity and stretchability of organic semiconductors is a vital step toward their application in future technologies.^[96,127] The blending with an insulating polymer promotes stretchability of the highly ordered fibril structures of semiconducting polymers by prevention of entanglement and

breakage at external stress.^[128] This concept is also applicable to intrinsically more rigid small molecular semiconductors, but blended with insulating elastomers to stimulate elasticity.

6. Semiconductor–Insulator Blends for Sensing

Charge carrier trapping at the interface between dielectric and OSC is one of the major obstacles for environmentally stable OFETs. Polar groups of the dielectric create trapping sites at the interface diminishing the carrier density in the conducting transistor channel. The trapped charge carriers can be released or refilled triggered by temperature increase, light illumination, and gas molecules penetrating the active layer.^[129–131] A larger number of potential trap states theoretically refine the sensitivity of an OFET-based sensor.^[132,133] Due to their environmental sensitivity and selectivity in stimulus response, OFETs have been proven as effective devices for the detection of a broad range of gases and chemical compounds present in vapor.^[134] Air-stable and reliable OFETs with phase separated dielectric polymer and OSC blends are attractive as low-cost sensors achieving detection capabilities comparable with metal–oxide-based devices.^[135,136] One strategy for applying phase separated blends is to maximize the interface area between dielectric and OSC, while maintaining the conductive properties of the active layer. In comparison to the performance of pristine organic semiconductors, phase separation in blends improves the electrical performance and environmental stability of OFETs, and also increases the sensitivity of corresponding chemical sensors.

6.1. Small Molecule–Dielectric Polymer Blends

Blending of small molecular OSC with insulating polymer enhances the OSC crystallinity and reduces the local trap den-

sity at the semiconductor/insulator interface.^[137] A low trap density at the interface is crucial for the operation stability and minimal bias stress of OFETs. An example is phase separated TIPS-pentacene/PS blends drop-cast on a poly(vinyl cinnamate) dielectric and exploited in OFET-based ammonia (NH₃) sensors (Figure 12a,c). Ammonia is one of the most studied stimuli among gas molecules.^[138] The OFETs demonstrated an excellent operational stability with subthreshold swing less than 100 mV per decade and on/off ratio of 10⁶ at a voltage swing of 3 V. The elastic OFETs (Figure 12b) were incorporated in a battery-powered electronic circuit for 12 h long continuous sensing of NH₃ vapor in air at a small power consumption of 50 nW. The NH₃ vapor exposure was monitored by an electronic system analyzing changes in bias voltages. The device performance and recovery are presented in Figure 12c.

Bilayer TIPS-pentacene/PS blends were also incorporated in NO₂ sensors in order to control the morphology and thickness of the semiconductor layer.^[139] The TIPS-pentacene crystalline layer structure was tuned by the spin-coating time of the blend. Short spin-coating times resulted in 1D crystals phase separated on top of the PS fraction, while longer optimized times yielded a continuous TIPS-pentacene layer of large 2D spherulites (Figure 12d,e). At short spin-coating times, residual solvent induced a convective flow in the drying droplet leading to the growth of the 1D crystals, whereas for a prolonged time, 2D crystal growth was observed at an optimum amount of the residual solvent. Films deposited at longer spin-coating times showed a higher charge carrier mobility of 0.65 cm² V⁻¹ s⁻¹ in comparison to 0.31 cm² V⁻¹ s⁻¹ at short processing times and almost twice higher sensitivity and response rates on exposure to 50 ppm NO₂ (Figure 12f). This improvement of the sensor performance was related to a better molecular assembly and lower thickness of the semiconductor layer. The thickness of the TIPS-pentacene layer decreased from almost 1 μm of the 1D crystal morphology to only 110 nm of the 2D spherulites.

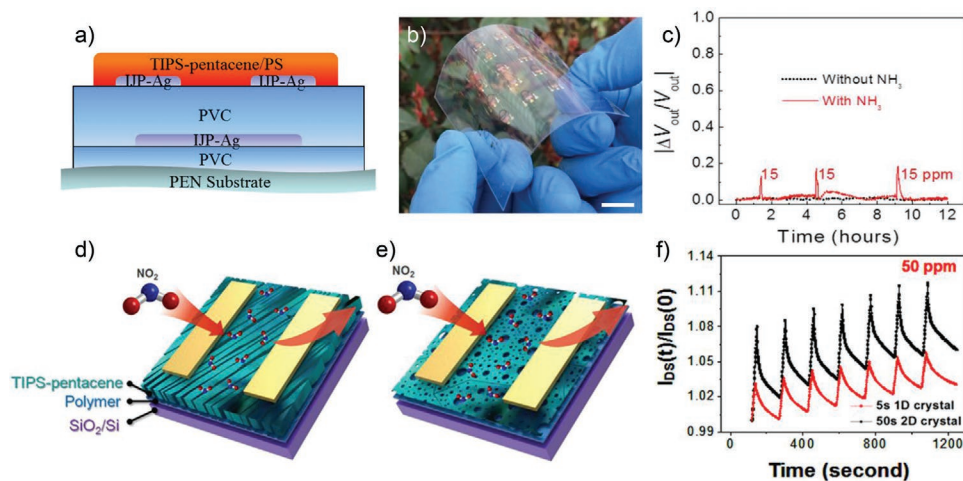


Figure 12. a) Device configuration of an OFET-based NH₃ sensor with TIPS-pentacene/PS blends drop-cast on a poly(vinyl cinnamate) dielectric, b) elastic sensor device (1 cm scale bar), c) sensing performance of the phase separated TIPS-pentacene/PS blend OFET with three NH₃ injections within 12 h. Reproduced with permission.^[138] Copyright 2016, Springer Nature. Schematic illustration of the OFET sensor devices with TIPS-pentacene/PS bilayer consisting of d) 1D crystals after short spin-coating time and e) 2D spherulitic structure obtained after long processing time. f) Sensing curves of OFET gas sensors with TIPS-pentacene/PS bilayer upon exposure to successive pulses of NO₂ (50 ppm) (red curve 1D crystals and black curve for 2D crystals). Reproduced with permission.^[139] Copyright 2019, Springer Nature.

Additionally, a porous structure of the thin 2D spherulites allowed the NO₂ molecules to penetrate the channel region more efficiently (Figure 12d,f).^[139]

Small molecule OSCs have been investigated not only in gas sensors, but also as light sensitive active layers attributed to their absorption spectra. Blending small molecules OSC with dielectric polymers is an efficient method to promote their stability and performance both in dark and light illumination.^[140] The OSC/dielectric interfacial area also plays a role in the performance of UV sensitive photosensors. The impact of two film structures on the photo-sensing properties of C8-BTBT and polylactide (PLA) blends was compared. The bilayer was processed by thermal evaporation of C8-BTBT on top of PLA, while a blend morphology was obtained by spin-coating both compounds together (Figure 13a). OFETs with the blend structure operated at one order of magnitude higher source–drain current and $I_{\text{light}}/I_{\text{dark}}$ ratio of 10⁵ as response to 365 nm light illumination in comparison to the bilayer. Additionally, the blend devices operated at a superior light detection limit of 0.02 mW cm⁻², while the bilayer OFETs demonstrated no difference in

response at 0.33 and 0.02 mW cm⁻². The better performance of the blend sensors was attributed to the more extended interfacial area between C8-BTBT and PLA. The polar carbonyl groups of PLA increased the number of trapping sites for charge carriers at a larger OSC/dielectric area enhancing in this way, the photosensitivity of the device. Furthermore, the domain size of C8-BTBT in blend films was smaller than in the evaporated layer. Due to the poorer crystallinity, the blend films revealed a lower detection limit and responsivity. The sensing performance of the blend was maintained even in printed OFETs that were incorporated in flexible UV sensors and bent at a radius of 300 μm (Figure 13b).^[141] An excellent photosensitivity of 10⁶ ($I_{\text{light}}/I_{\text{dark}}$) combined with operational air stability and a detection limit of only 0.12 mW cm⁻² has been presented for C5-BTBT:PI (polyimide) blended films in UV-sensitive transistors (Figure 13c). The use of PI as strong electron withdrawing polymer allowed the fabrication of hysteresis-free photosensors with reduced response time by almost 16 times compared to the pure C5-BTBT film.^[142] By applying double-layered polymer blend/SiO₂ gate dielectric, the photosensitivity of the

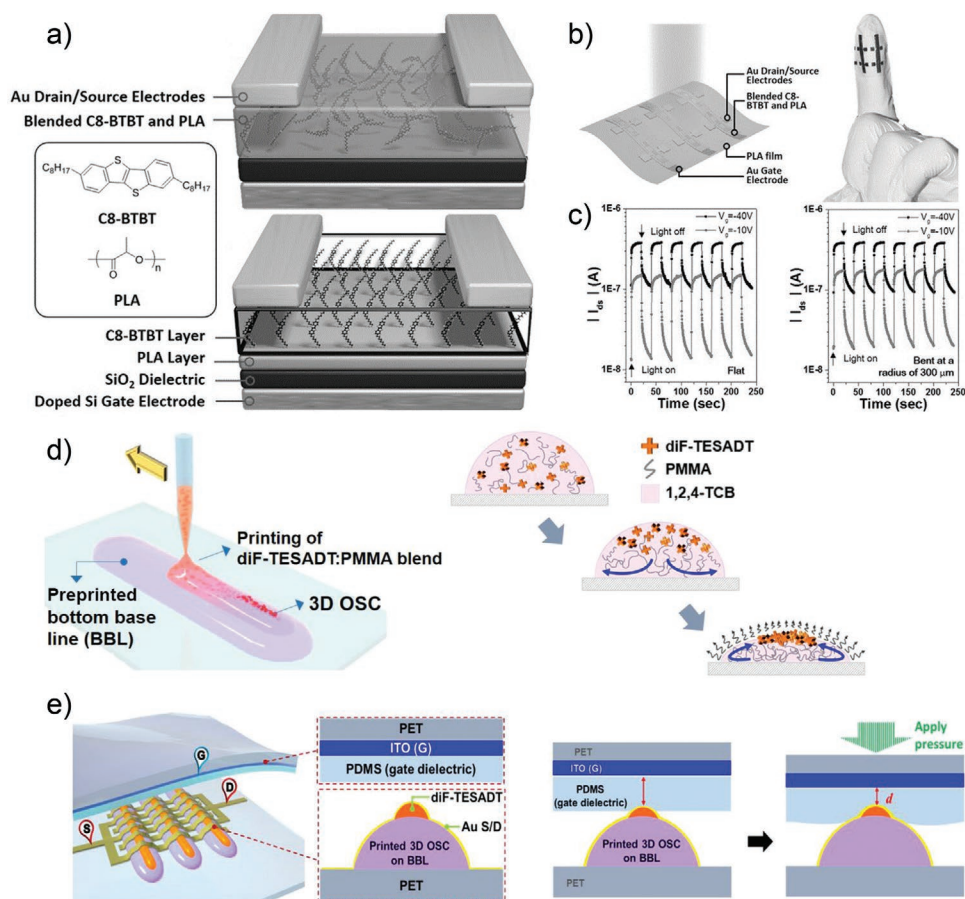


Figure 13. a) Schematic illustration of blended (top) and layered (bottom) structure of UV sensitive photosensors based on C8-BTBT and PLA, b) setup of inkjet printed and flexible photosensors containing the blend film of C8-BTBT and PLA (left) and application on a finger (right), c) photocurrent response to periodic light pulses measured in flat (left) and bended geometries (right). Reproduced with permission.^[141] Copyright 2017, Wiley-VCH. Schematic illustrations of d) printing of the diF-TES-ADT/PMMA blend solution onto the preprinted PMMA baseline (BBL) (left) and centro-apical self-organization of the diF-TES-ADT molecules in a line-printed diF-TES-ADT/PMMA blend during solvent evaporation (right), e) OFET pressure sensor consisting of a bottom diF-TES-ADT layer and PDMS top-gate (left) and pressure-sensing process (right). Reproduced with permission.^[144] Copyright 2017, American Chemical Society.

C5-BTBT:PI device further increased to 10^7 and the detection limit to 0.11 mW cm^{-2} . The polymer dielectric was composed of a poly(4-vinylphenol) and polymethylsilsesquioxane blend (PVP:pMSSQ). The blend dielectric film was hydrophobic, electroneutral, and cross-linked, bearing a moderate capacitance for a hysteresis-free and low voltage operation which are important for photo memory elements.^[143]

Phase separated OSC/dielectric polymer blends were also exploited in elastic high sensitivity pressure sensors for real-time monitoring of radial artery pulse waves. The pressure sensitive OFETs in top gate configuration were based on an elastic PDMS dielectric layer and transparent ITO gate electrode laminated with a polyethylene foil (Figure 13d).^[144] The active layer of the transistor was printed on a flexible polyethylene substrate and consisted of a vertically phase separated diF-TES-ADT/PMMA blend (Figure 13d). The p-type diF-TES-ADT phase separated on top of PMMA in a half-cylindrical printed line (Figure 13d). The semiconducting layer was in direct contact with the PDMS top-gate dielectric so that the capacitance changed under pressure. The smaller thickness of the elastic PDMS dielectric under pressure increased the areal capacitance and the source-drain current linearly (Figure 13e). The printed active layer showed over ten times higher sensor sensitivity (1.07 kPa^{-1}) in comparison to spin-coated blend films (0.09 kPa^{-1}). The printed sensors operated a rapid response, relaxation time of 18 ms, and excellent reliability even after 1000 cycles of repeatedly loading and unloading a pressure of 1.0 kPa at a frequency of 0.5 Hz.^[144]

6.2. Conjugated-Dielectric Polymer Blends

Incorporation of a blend of two polymers as the active film in stimuli-responsive OFETs opens the possibility for additional design strategies for sensors. Factors such as M_w , blending ratio, phase separation (lateral, vertical or both), layer porosity, deposition and post-modification of the film, main chain composition, and conformation, affect the sensing performance. Understanding the mechanism of phase separation during processing and the target stimuli response of the organic semiconductor permits an optimization of the sensitivity, recovery, and operation voltage of the OFET-based sensors. On the one hand, phase separation in polymer blends is more complex in comparison to polymer-small molecule mixtures, but on the other hand, polymer blends are more promising to enhance the elasticity of the devices. As mentioned before, one of the most studied stimuli among gas molecules is NH_3 . Sensors based on P3HT/PS bilayer OFETs, where PS was located at the top and P3HT at the bottom, revealed comparable responsivity and higher sensitivity in selective NH_3 detection at low concentrations (from 5 to 50 ppm) in comparison to devices with pristine P3HT. The superior sensing performance of the P3HT/PS blend was associated with higher charge carrier trapping at the larger interface between dielectric and semiconductor, as already observed for small molecules OSC blends. During exposition to NH_3 vapor, the gas diffusion through the active layer induced dipole-charge interactions between NH_3 and P3HT which eased the number of free charge carriers and consequently the source-drain current (Figure 14a). The phase sep-

aration in the film resulted in an extended P3HT/PS interface leading to a better sensitivity of the sensor in comparison to pure P3HT. The blend devices gave comparable signal response even after 40 days in air thanks to encapsulation of the P3HT layer by PS (Figure 14a).^[145]

A detection limit of only 0.7 ppb was achieved for NO_2 OFET sensors based on one-step deposited P3HT/PMMA bilayer by optimizing concentration and M_w of PMMA (Figure 14b).^[136] The devices exhibited a responsivity of 1481% at 30 ppm and 487% at 0.5 ppm. In contrast, the responsivity of bilayers obtained by sequential deposition of each polymer (Figure 14b) was lower, reaching values of only 116% at 30 ppm and 22% at 0.5 ppm. The blend morphology and phase separation at 1:60 P3HT/PMMA weight ratio as well as the final sensing response strongly depended on the M_w of PMMA. At 30 ppm NO_2 , the responsivity gradually increased from 254% for 15 kDa to 1481% for 120 kDa, while a further rise in M_w of PMMA decreased the value to 340% for 350 kDa. The best device performance was found for 120 kDa PMMA through to the most homogeneous P3HT morphology in the blend film. The small and high M_w were responsible for a discontinuous microstructure of P3HT (Figure 14c) and consequently, for poor charge carrier mobility as well as sensing performance.^[136]

As mentioned earlier, responsivity, sensitivity, and faster response/recovery times of OFET-based gas sensors are strongly affected by the surface area of the OSC/dielectric active layer, also in the case of conjugated polymers. Spin coating of P3HT/PS blends under controlled humidity ($\approx 60\%$) yielded highly structured porous films with large interfacial area (Figure 14d).^[130] The film porosity originated from water condensation during film deposition and improved the interaction between stimuli gas molecules and conjugated polymer in the transistor active layer (Figure 14e). The porous film morphology allowed more efficient diffusion of the NO_2 molecules into the layer, faster switching speeds, and enhanced gas sensitivity in comparison to dense P3HT/PS films (Figure 14f). An identical effect was observed for C8-BTBT/PS films.

In another approach, phase separation was applied in blends to fabricate ultra-thin semiconducting polymer films that are particularly attractive for sensitive and fast-responding gas sensors. In spin-coated P3HT/PMMA blends, a thin semiconducting layer vertically phase separated on the top of the film.^[146] To obtain a continuous thin film consisting of pure P3HT, the phase separated bilayer was lifted off and flipped to wash off the PMMA layer by acetone. The thickness of the final semiconducting film was controlled in the range from 2.0–7.4 nm by variation of the P3HT/PMMA ratio. In the next step, the separated P3HT thin films were placed on a SiO_2 dielectric of an OFET sensor. The small film thickness mainly contributed to a fast gas diffusion to the active layer/dielectric interface and a quick response as well as recovery of the sensor. The highest response to 10 ppm NH_3 exposure was observed for the lowest film thickness of 2.0 nm in a 31% decrease in drain-source current in comparison to unexposed devices (Figure 15a). The weakest response was observed for the 7.4 nm thick film with only 6.9% current decline, but without significant difference in response time (Figure 14b). The recovery time increased from 80 s for 2.0 nm to 123 s for 7.4 nm thick films which was associated

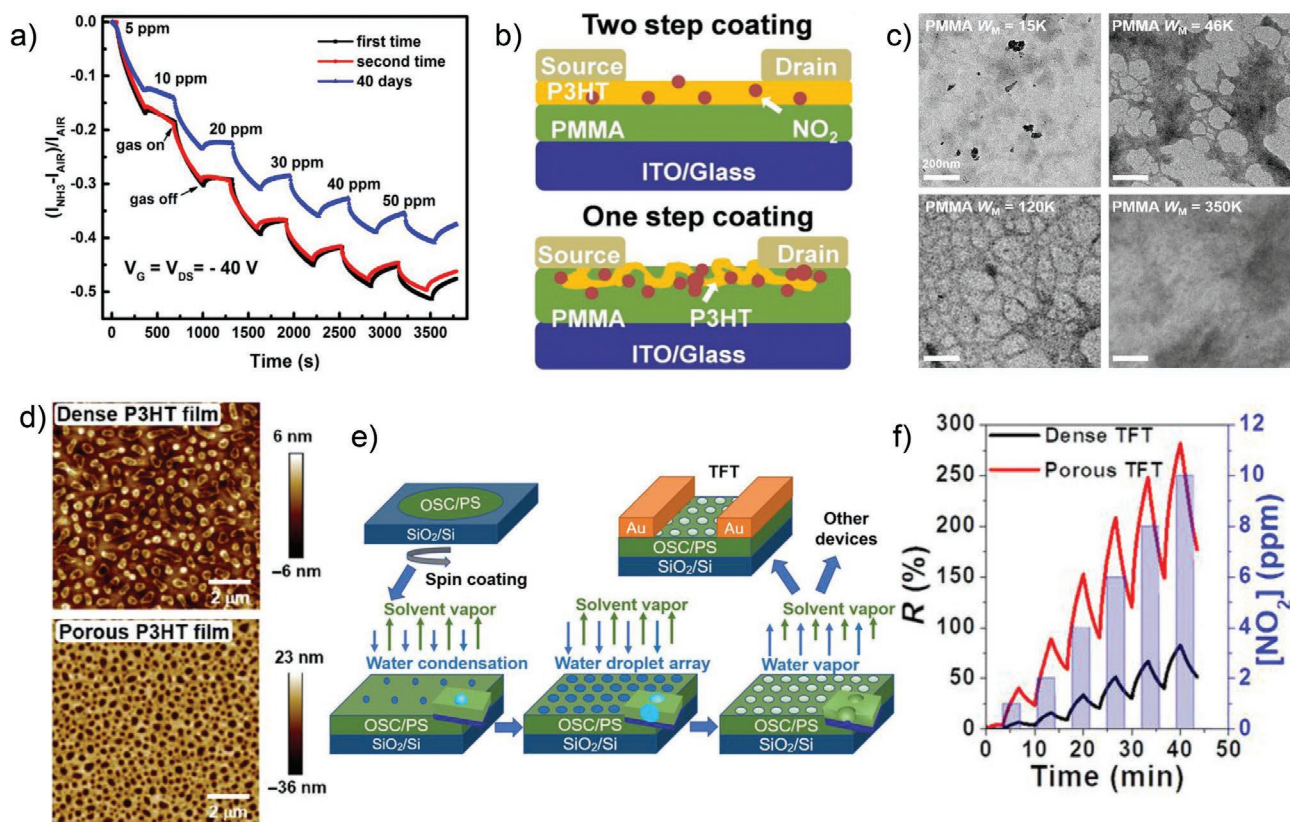


Figure 14. a) Response curves of P3HT/PS blend devices with changes in drain–source current during stepwise increase of the NH₃ vapor concentration. Reproduced with permission.^[145] Copyright 2016, Elsevier. b) Schematic device configuration obtained by one-step and two-step deposition of P3HT/PMMA blends, c) TEM images of P3HT/PMMA blends with different M_w of PMMA. The darker phase is associated with areas of higher P3HT density, whereas brighter ones are PMMA rich areas. Scale bar for all images is 200 nm. Reproduced with permission.^[136] Copyright 2019, American Chemical Society. d) AFM images of dense and porous P3HT films, e) scheme of film deposition, f) real-time responsivity to dynamic NO₂ concentrations. Reproduced with permission.^[130] Copyright 2020, American Association for the Advancement Science.

with longer NH₃ diffusion time (Figure 15b). This study confirmed high potential of ultra-thin continuous semiconductor films for fast and sensitive sensors.^[146]

An excellent response of 28.6% in the drain–source current at only 0.1 ppm NH₃ has been reported for nanofibrils of a helical block copolymer (PPI-(DMAENBA)-b-P3HT) that comprised

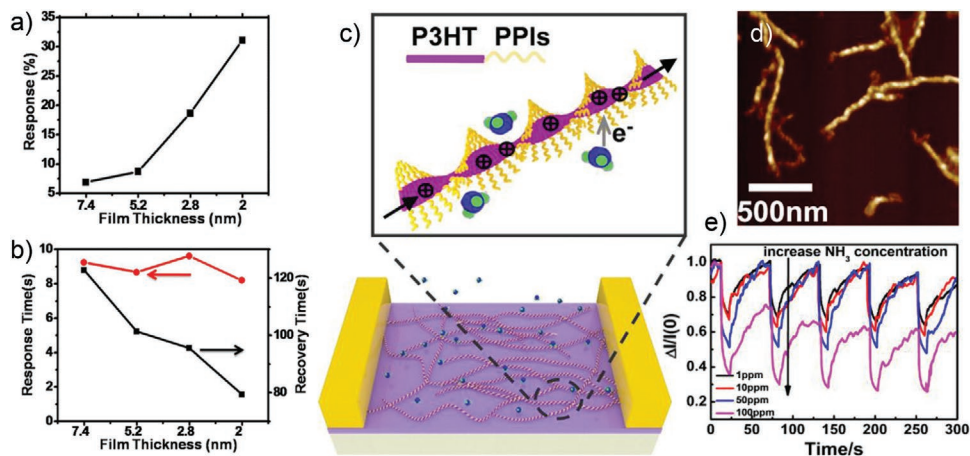


Figure 15. a) Drain–source current of responsive P3HT/PMMA-based sensor and b) recovery time as a function of P3HT layer thickness. Reproduced with permission.^[146] Copyright 2018, Elsevier. c) Scheme of helical PPI-(DMAENBA)-b-P3HT polymer structure and its self-assembly in OFET based-sensor devices, d) AFM image of self-assembled PPI-(DMAENBA)-b-P3HT fibers, e) and its drain-current response at different ammonia concentrations. Reproduced with permission.^[147] Copyright 2018, American Chemical Society.

conjugated and non-conjugated units (Figure 15c).^[147] This performance was attributed to the large surface-to-volume ratio of the helical polymer chains. In comparison to pristine tightly packed P3HT chains, the helical arrangement exposed π -electrons of the conjugated backbone and enlarged in this way, the interaction area of the PPI(-DMAENBA)-b-P3HT copolymer (Figure 15d). The configuration of the helical fibers was optimized by the type of solvent and PMMA:PPI(-DMAENBA)-b-P3HT ratio in a blend. The blend was used to control the film formation of PPI(-DMAENBA)-b-P3HT by micro phase separation (Figure 15c). After removing PMMA by solvent, a thin helical fiber film with a much faster response and recovery time was achieved in comparison to fiber morphologies of other non-helical conjugated polymers such as P3HT or P3HT-b-PHA (Figure 15e). The selectivity of OFET sensors can be further increased by attaching side groups to the P3HT-copolymer to promote interactions with the target gas molecules.^[147,148]

The chain conformation of core-shell structured poly(3-hexylthiophene)-poly(hexadecyloxyallene) (P3HT-b-PHA) was also controlled by phase separation to incorporate the polymer as active layer in OFET-based deep ultraviolet photodetectors. The microfibrillar morphology of the copolymer was achieved by a similar PMMA etching method as described in the previous case. Due to the micro phase separation, the PHA shell

absorbed deep-UV light at 254 nm (Figure 16a).^[149] After the diffusion to the core/shell interface, the generated excitons separated into electrons and holes driven by an external bias. The P3HT-b-PHA OFET sensors achieved a great $I_{\text{light}}/I_{\text{dark}}$ ratio of 4000, responsivity of 120 AW^{-1} , and external quantum efficiency of 4.97×10^4 which was even higher than for graphene/metal oxide-based devices.^[150] The devices also demonstrated pronounced selective photoresponse to deep UV irradiation and almost no reaction to light in the range between 300 to 800 nm unlike devices containing bulk-type P3HT-b-PHA (Figure 16b). To illustrate the imaging capabilities of the P3HT-b-PHA fibers, flexible deep UV and solar blind sensors were constructed composed of 10×10 pixels of a flexible OFET array (Figure 16c,d).

As presented in the last examples, phase separation in blends was exploited not only to control the conformation of molecules in the active layer, but also to tune the semiconducting film morphology. Humidity sensors with donor-acceptor polymer PBIBDF-BT (bis(2-oxindolin-3-ylidene)-benzodifuran-dione and bithiophene-based low band-gap polymer) as porous active film exhibited the shortest response time among other organic semiconductor-based devices.^[151] The pore size in the films was controlled by varying the weight ratio of PBIBDF-BT-PBA insulator blends and by the removal process of the insulator fraction from the phase separated film. After washing out

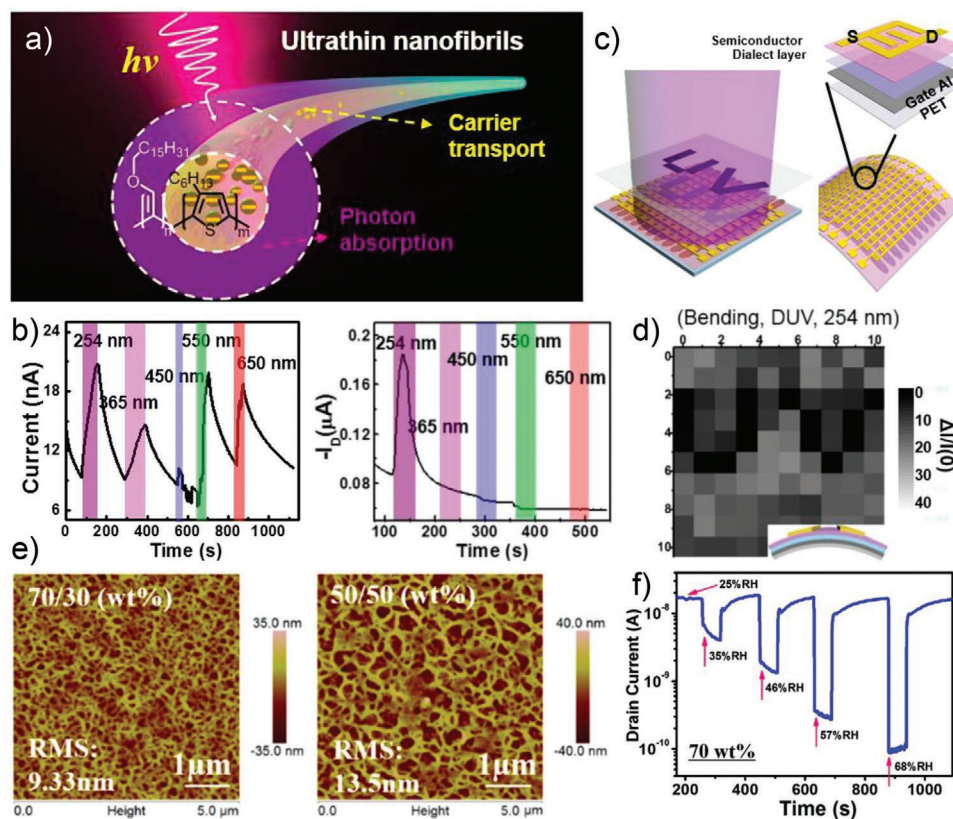


Figure 16. a) Scheme of P3HT-b-PBA core-shell structure, b) photocurrent responses for bulk (left) and core-shell structured (right) P3HT-b-PBA films, c) scheme of flexible OFET-based optical sensor array, d) sensor map tested for OFET array under bending. Reproduced with permission.^[149] Copyright 2020, American Chemical Society. e) AFM images for acetone rinsed PBIBDF-BT porous films at different PBIBDF-BT:PBA weight ratios, f) changes in drain current at different relative humidity levels from 25% to 68% for blend film with 70 wt% PBIBDF-BT. Reproduced with permission.^[151] Copyright 2017, American Chemical Society.

PBA, the resulting porous PBIBDF–BT film revealed average pore diameters ranging from 84 to 154 nm depending on the polymer fraction (Figure 16e). The highest sensitivity of 415, defined as ratio of the original source–drain current before and after exposure to water vapor (I_0/I_{H_2O}), and the fastest recovery time of 45 s was observed for relative humidity in the range of 32–69% (Figure 16f). This pronounced sensitivity was achieved for the largest pore size through an extended interaction area between water and semiconductor.^[151] The same materials and device fabrication were used for OFET-based NH₃ sensors. In comparison to a homogenous film, the porous PBIDF–BT morphology showed significantly higher sensitivity, shorter response/recovery time, and detection limit of 0.5 ppm. Due to the ambipolar character of the semiconducting polymer, the sensor responded to NH₃ in the hole and electron regime.^[152] Similar blends of PBA:PBTDIBDF-5 (donor–acceptor copolymer) were incorporated in flexible low-voltage organic phototransistors with an ultralow detection limit of 0.03 mW cm⁻² and responsivity of 128 A W⁻¹.^[153] The pronounced sensitivity of the devices was attributed to the synergistic effect of chemical and physical blending. Chemical blending was realized by selecting specific building blocks of the conjugated backbone to adjust the OSC bandgap energy level of copolymer. Physical blending was performed by addition of a dielectric polymer into the active layer to increase the trap density.^[153]

The blend composition can be adjusted to exploit OFETs also for temperature sensing. A dielectric polymer with a large thermal expansion coefficient was selected for a desired temperature range, as in the case of P3HT/PE (polyethylene) blends. The charge carrier mobility of corresponding reversible thermo-responsive OFET switches declined by 30% by changing the temperature from 30 °C to 120 °C in contrast to pristine P3HT devices. The mobility changes were attributed to the thermal expansion of the PE matrix which increased the distance between the P3HT conducting domains. It was concluded that such sensors might be applied in overheating protection.^[129]

As discussed in this section, the concept of phase separated blends in OFET-based sensors allows to enlarge the interfacial area between the semiconducting and insulating fractions to tune the sensing properties of the semiconductors and construct thin and flexible devices. Defined phase separation significantly improves the sensor performance in comparison to pure semiconductors such as response and recovery time, sensitivity, and selectivity.

7. Conclusions and Outlook

As discussed in this review, blending organic semiconductors with insulating polymers circumvents their limitations in OFETs of low charge carrier mobilities and poor environmental stability and opens the doors toward a broad range of novel applications (Figure 17). The OFET performance of conjugated polymers and small molecules is promoted by the incorporation of an insulating thermoplastic polymer or elastomer during solution processing of the active film. By adjustment of the blend composition and processing conditions, it is possible to well-tune the phase separation and blend film morphology. Interconnected domains of the organic semiconductor phase provide precisely established pathways for the charge carriers resulting in preservation or even improvement of the transistor performance because of enhanced morphology and higher order of the conjugated molecules in the blend film. Among these beneficial features, one can distinguish: 1) increase of the charge carrier mobility related to higher molecular order of the semiconductor driven by a defined phase separation; 2) controlled interfacial trapping in sensors and OFETs through vertically phase separated bilayer structure; 3) reduced consumption of the semiconducting material required for a continuous film interconnecting the electrodes; 4) long-term environmental stability thanks to encapsulation of the semiconductor bottom layer; 5) higher mechanical elasticity of the active film by absorption of the mechanical stress by the insulating matrix;

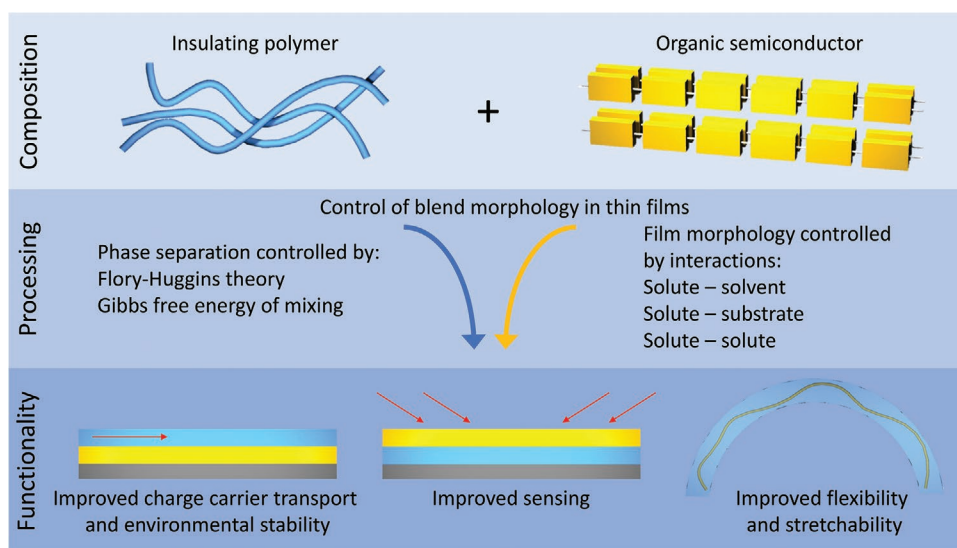


Figure 17. Schematic illustration of the concept of blending organic semiconductors with insulating polymers and controlling the blend morphology in their films. This approach improves the functionality of the organic semiconductor in transistors, sensors, and flexible applications.

and 6) superior sensing performance of the semiconductor due to higher interfacial area to the insulating phase. These device improvements overcome intrinsic limitation of neat organic semiconductors and allow the application of these materials as blends in high performance organic transistors for next generation technologies that require elasticity, stretchability, or sensing ability.

To further exploit the great potential of this concept toward practical applications in electronics, important requirements need to be fulfilled. One major issue is related to mechanical reliability and fatigue behavior of the blend active films in the elastic transistors. Although their improved mechanical properties in comparison to neat organic semiconductors have been proven on laboratory scale, the long-term electronic performance under mechanical stress has not been studied. This includes monitoring of structural and electronic changes in the blend films over continuous deformation cycles and long-term constant deformation that better reflect real conditions during applications. The long-term changes can comprise fluctuations in the molecular organization of the organic semiconductor and breakages at the interphases between both fractions leading to decrease in charge carrier transport and lower device performance. Further issues are charge carrier trapping by emerging structural defects generating bias stress and lower charge carrier mobilities. Structural changes also concern the insulating matrix. Thermoplastic polymers such as PS and PMMA that are mainly applied for the blends, possess a satisfying Young's modulus but are rather brittle and show a low elongation at break not permitting large deformations. On the other side, reinforced elastomers undergo a Mullins stress softening during the initial elongation due to disruptions in the polymer network leading to irreversible permanent set. For this reason, it is inevitable to select the suitable insulating polymer for the blend regarding the expected mechanical stress and strains during deformation. To meet long-term requirements, possibly other blend compositions and insulating polymers will need to be identified in future.

Another aspect concerns ease and continuous solution processing of thin blend films. As a technique of great potential, meniscus-guided coating is known to induce high directional order in neat organic semiconductors. Another effective and up-scalable processing method is ink-jet printing. However, only few reports describe these techniques for the deposition of organic semiconductor/insulator blends, whereby film processing of active blends on the large scale remains challenging and an essential prerequisite for practical electronic devices. The main challenge is the optimization of the processing conditions to accordingly control the blend morphology and molecular order of the semiconductor to maintain the desired properties. This is especially the case when the blend solution is deposited on patterned surfaces of varied surface energies of the device. On the other hand, meniscus-guided coating allows to set a broad range of additional processing parameters such as substrate and solution temperature as well as coating speed and offers in this way, a significantly higher control over the blend film morphology than by traditional processing methods.

Although small molecule semiconductors showed superior electronic properties in blends, their application in flexible and stretchable devices has remained limited to only few

reported cases. The main reason for this restriction is their pronounced brittleness resulting in severe cracking at even small deformation of the electronic devices. The question is how small molecule semiconductors can be incorporated into blends to maintain their great electronic performance at mechanical deformation. The solution might be a fine distribution of the small molecules within the insulating polymer matrix instead of a complete phase separation of the brittle semiconducting layer. In the case of blends with conjugated polymers, typically fibrous structures are self-assembled homogeneous within the insulating matrix that acts as stress absorber during deformation. A similar approach might be applicable to small molecules by adjusting the processing conditions to control their structure formation of a fine network in the blend. The gained insights for crystalline small molecules can be later transferred to other classes of semiconducting materials such as perovskites and metal oxide semiconductors that also suffer from not suitable mechanical properties and poor stability at mechanical load. This concept can be extended not only to other active materials, but also to different types of electronic devices beyond transistors. High electric performance linked with environmental and mechanical stability is also required in light-emitting diodes and solar cells. However, both device categories contain a completely different geometry in comparison to transistors. In these devices, the electrodes are diode-like arranged and the charge carrier transport occurs perpendicular to the substrate. In this case, a phase separated bilayer structure between semiconductor and insulator hinders the migration of charges between electrodes. To ensure transport, an intermixed blend morphology is required such as of conjugated polymer fibers in the insulator matrix, whereby the fiber pathways need to be homogeneously distributed over the entire film bulk to interconnect the electrodes. This morphology allows the absorption of external stress by the insulator matrix and charge transport through the semiconducting fibers in a diode-like device geometry. Additionally, the embedded fibers are protected against environmental conditions.

In conclusion, the strategy of blending electronically active materials with insulators has been proven to improve key properties of the semiconductors and bears great potential for elastic electronics. For the next step into application, practical problems such as reliability and large area processing need to be solved.

Acknowledgements

L.J. and M.B. contributed equally to this work. M.B. and T.M. acknowledge the Foundation for Polish Science financed by the European Union under the European Regional Development Fund (POIR.04.04.00-00-3ED8/17). W.P. acknowledges the National Science Centre, Poland through the grants UMO-2015/18/E/ST3/00322 and UMO-2019/33/B/ST3/1550.

Open access funding enabled and organized by Projekt DEAL.

Conflict of Interest

The authors declare no conflict of interest.

Keywords

blends, flexible field-effect transistors, organic electronics, organic semiconductors, sensors

Received: June 7, 2021
Revised: August 29, 2021
Published online:

- [1] H. Sirringhaus, *Adv. Mater.* **2014**, *26*, 1319.
- [2] G. Schweicher, G. Garbay, R. Jouclas, F. Vibert, F. Devaux, Y. H. Geerts, *Adv. Mater.* **2020**, *32*, 1905909.
- [3] G. Wang, M. A. Adil, J. Zhang, Z. Wei, *Adv. Mater.* **2019**, *31*, 1805089.
- [4] Y. van de Burgt, A. Melianas, S. T. Keene, G. Malliaras, A. Salleo, *Nat. Electron.* **2018**, *1*, 386.
- [5] Y. Yao, H. Dong, W. Hu, *Adv. Mater.* **2016**, *28*, 4513.
- [6] Ł. Janasz, J. Ulański, W. Pisula, in *Solution-Processable Components for Organic Electronic Devices* (Eds: B. Luszczynska, J. Ulanski), Wiley-VCH, Weinheim, Germany **2019**, pp. 365–412.
- [7] Y. Zhao, Y. Guo, Y. Liu, *Adv. Mater.* **2013**, *25*, 5372.
- [8] X. Yu, T. J. Marks, A. Facchetti, *Nat. Mater.* **2016**, *15*, 383.
- [9] L. Tao, E. Cinquanta, D. Chiappe, C. Grazianetti, M. Fanciulli, M. Dubey, A. Molle, D. Akinwande, *Nat. Nanotechnol.* **2015**, *10*, 227.
- [10] R. Coehoorn, P. A. Bobbert, in *Physics of Organic Semiconductors*, 2nd ed. (Eds: W. Brütting, C. Adachi), Wiley-VCH, Weinheim, Germany **2013**, pp. 155–199.
- [11] I. Kymissis, *Organic Field Effect Transistors: Theory, Fabrication and Characterization*, 1st ed., Integrated Circuits and Systems, Springer, Boston, MA **2009**.
- [12] Y. Lee, H. Zhou, T.-W. Lee, *J. Mater. Chem. C* **2018**, *6*, 3538.
- [13] A. T. Kleinschmidt, D. J. Lipomi, *Acc. Chem. Res.* **2018**, *51*, 3134.
- [14] R. Devarapalli, S. B. Kadambi, C.-T. Chen, G. R. Krishna, B. R. Kammari, M. J. Buehler, U. Ramamurty, C. M. Reddy, *Chem. Mater.* **2019**, *31*, 1391.
- [15] J. A. Rogers, T. Someya, Y. Huang, *Science* **2010**, *327*, 1603.
- [16] Y. Lee, M. Shin, K. Thiyagarajan, U. Jeong, *Macromolecules* **2016**, *49*, 433.
- [17] H. Ling, S. Liu, Z. Zheng, F. Yan, *Small Methods* **2018**, *2*, 1800070.
- [18] G. De Luca, W. Pisula, D. Credgington, E. Treossi, O. Fenwick, G. M. Lazzerini, R. Dabirian, E. Orgiu, A. Liscio, V. Palermo, K. Müllen, F. Cacialli, P. Samori, *Adv. Funct. Mater.* **2011**, *21*, 1279.
- [19] N. E. Persson, P.-H. Chu, M. McBride, M. Grover, E. Reichmanis, *Acc. Chem. Res.* **2017**, *50*, 932.
- [20] R. Ma, S.-Y. Chou, Y. Xie, Q. Pei, *Chem. Soc. Rev.* **2019**, *48*, 1741.
- [21] M. Wang, P. Baek, A. Akbarinejad, D. Barker, J. Travas-Sejdic, *J. Mater. Chem. C* **2019**, *7*, 5534.
- [22] Y. Qian, X. Zhang, L. Xie, D. Qi, B. K. Chandran, X. Chen, W. Huang, *Adv. Mater.* **2016**, *28*, 9243.
- [23] M. Ashizawa, Y. Zheng, H. Tran, Z. Bao, *Prog. Polym. Sci.* **2020**, *100*, 101181.
- [24] J. Zhao, Z. Chi, Z. Yang, X. Chen, M. S. Arnold, Y. Zhang, J. Xu, Z. Chi, M. P. Aldred, *Nanoscale* **2018**, *10*, 5764.
- [25] S. E. Root, S. Savagatrup, A. D. Printz, D. Rodriguez, D. J. Lipomi, *Chem. Rev.* **2017**, *117*, 6467.
- [26] A. D. Scaccabarozzi, N. Stingelin, *J. Mater. Chem. A* **2014**, *2*, 10818.
- [27] B. Kang, F. Ge, L. Qiu, K. Cho, *Adv. Electron. Mater.* **2017**, *3*, 1600240.
- [28] S. Riera-Galindo, F. Leonardi, R. Pfattner, M. Mas-Torrent, *Adv. Mater. Technol.* **2019**, *4*, 1900104.
- [29] L.-H. Chou, Y. Na, C.-H. Park, M. S. Park, I. Osaka, F. S. Kim, C.-L. Liu, *Polymer* **2020**, *191*, 122208.
- [30] A. Campos, S. Riera-Galindo, J. Puigdollers, M. Mas-Torrent, *ACS Appl. Mater. Interfaces* **2018**, *10*, 15952.
- [31] M. T. Chung, Z. E. Tsay, M. H. Chi, Y. W. Wang, *Thin Solid Films* **2017**, *638*, 441.
- [32] C. Liu, Y. Li, M. V. Lee, A. Kumatani, K. Tsukagoshi, *Phys. Chem. Chem. Phys.* **2013**, *15*, 7917.
- [33] D. Kwak, H. H. Choi, B. Kang, D. H. Kim, W. H. Lee, K. Cho, *Adv. Funct. Mater.* **2016**, *26*, 3003.
- [34] A. Pérez-Rodríguez, I. Temiño, C. Ocal, M. Mas-Torrent, E. Barrera, *ACS Appl. Mater. Interfaces* **2018**, *10*, 7296.
- [35] G. Lu, J. Blakesley, S. Himmelberger, P. Pingel, J. Frisch, I. Lieberwirth, I. Salzmann, M. Oehzelt, R. Di Pietro, A. Salleo, N. Koch, D. Neher, *Nat. Commun.* **2013**, *4*, 1588.
- [36] M. Chang, Z. Su, E. Egap, *Macromolecules* **2016**, *49*, 9449.
- [37] T. Ohe, M. Kuribayashi, A. Tsuboi, K. Satori, M. Itabashi, K. Nomoto, *Appl. Phys. Express* **2009**, *2*, 121502.
- [38] S. Y. Cho, J. M. Ko, J. Lim, J. Y. Lee, C. Lee, *J. Mater. Chem. C* **2013**, *1*, 914.
- [39] J. Smith, R. Hamilton, I. McCulloch, N. Stingelin-Stutzmann, M. Heeney, D. D. C. Bradley, T. D. Anthopoulos, *J. Mater. Chem.* **2010**, *20*, 2562.
- [40] D. T. James, B. K. C. Kjellander, W. T. T. Smaal, G. H. Gelinck, C. Combe, I. McCulloch, R. Wilson, J. H. Burroughes, D. D. C. Bradley, J.-S. Kim, *ACS Nano* **2011**, *5*, 9824.
- [41] L. J. Richter, D. M. DeLongchamp, A. Amassian, *Chem. Rev.* **2017**, *117*, 6332.
- [42] S. Goffri, C. Müller, N. Stingelin-Stutzmann, D. W. Breiby, C. P. Radano, J. W. Andreasen, R. Thompson, R. A. J. Janssen, M. M. Nielsen, P. Smith, H. Sirringhaus, *Nat. Mater.* **2006**, *5*, 950.
- [43] A. C. Arias, F. Endicott, R. A. Street, *Adv. Mater.* **2006**, *18*, 2900.
- [44] E. Song, B. Kang, H. H. Choi, D. H. Sin, H. Lee, W. H. Lee, K. Cho, *Adv. Electron. Mater.* **2016**, *2*, 1500250.
- [45] T. Shen, H. Zhou, J. Xin, Q. Fan, Z. Yang, J. Wang, T. Mei, X. Wang, N. Wang, J. Li, *Appl. Surf. Sci.* **2019**, *498*, 143822.
- [46] J. Kang, N. Shin, D. Y. Jang, V. M. Prabhu, D. Y. Yoon, *J. Am. Chem. Soc.* **2008**, *130*, 12273.
- [47] S. Wang, Z. Chen, Y. Wang, *Chem. Commun.* **2015**, *51*, 765.
- [48] J. J. Michels, A. Kunz, H. S. Dehsari, K. Asadi, P. W. M. Blom, in *Solution-Processable Components for Organic Electronic Devices* (Eds: B. Luszczynska, J. Ulanski), Wiley-VCH, Weinheim, Germany **2019**, pp. 227–258.
- [49] S. Coveney, *Fundamentals of Phase Separation in Polymer Blend Thin Films*, 1st ed., Springer Theses, Springer International Publishing, Cham, Switzerland **2015**.
- [50] Y. Liu, *J. Appl. Polym. Sci.* **2013**, *127*, 3279.
- [51] M. Kastler, W. Pisula, F. Laquai, A. Kumar, R. J. Davies, S. Balushev, M.-C. Garcia-Gutiérrez, D. Wasserfallen, H.-J. Butt, C. Riekel, G. Wegner, K. Müllen, *Adv. Mater.* **2006**, *18*, 2255.
- [52] V. Coropceanu, J. Cornil, D. A. da Silva Filho, Y. Olivier, R. Silbey, J.-L. Brédas, *Chem. Rev.* **2007**, *107*, 926.
- [53] A. Facchetti, *Chem. Mater.* **2011**, *23*, 733.
- [54] A. Köhler, H. Bässler, *Electronic Processes in Organic Semiconductors*, Wiley-VCH, Weinheim, Germany **2015**.
- [55] K. S. Park, J. J. Kwok, R. Dilmurat, G. Qu, P. Kafle, X. Luo, S.-H. Jung, Y. Olivier, J.-K. Lee, J. Mei, D. Beljonne, Y. Diao, *Sci. Adv.* **2019**, *5*, eaaw7757.
- [56] K. Zhang, Z. Wang, T. Marszalek, M. Borkowski, G. Fytas, P. W. M. Blom, W. Pisula, *Mater. Horiz.* **2020**, *7*, 1631.
- [57] H. N. Tsao, K. Müllen, *Chem. Soc. Rev.* **2010**, *39*, 2372.
- [58] N. A. Minder, S. Ono, Z. Chen, A. Facchetti, A. F. Morpurgo, *Adv. Mater.* **2012**, *24*, 503.
- [59] L. Ying, F. Huang, G. C. Bazan, *Nat. Commun.* **2017**, *8*, 14047.
- [60] R. Noriega, J. Rivnay, K. Vandewal, F. P. V. Koch, N. Stingelin, P. Smith, M. F. Toney, A. Salleo, *Nat. Mater.* **2013**, *12*, 1038.

- [61] J.-S. Kim, J.-H. Kim, W. Lee, H. Yu, H. J. Kim, I. Song, M. Shin, J. H. Oh, U. Jeong, T.-S. Kim, B. J. Kim, *Macromolecules* **2015**, *48*, 4339.
- [62] T. Kaimakamis, C. Pitsalidis, A. Papamichail, A. Laskarakis, S. Logothetidis, *RSC Adv.* **2016**, *6*, 97077.
- [63] T. Shen, H. Zhou, X. Liu, Y. Fan, D. D. Mishra, Q. Fan, Z. Yang, X. Wang, M. Zhang, J. Li, *ACS Omega* **2020**, *5*, 10891.
- [64] N. Shin, J. Kang, L. J. Richter, V. M. Prabhu, R. J. Kline, D. A. Fischer, D. M. DeLongchamp, M. F. Toney, S. K. Satija, D. J. Gundlach, B. Purushothaman, J. E. Anthony, D. Y. Yoon, *Adv. Funct. Mater.* **2013**, *23*, 366.
- [65] K. Zhang, T. Marszalek, P. Wucher, Z. Wang, L. Veith, H. Lu, H. Räder, P. M. Beaujuge, P. W. M. Blom, W. Pisula, *Adv. Funct. Mater.* **2018**, *28*, 1805594.
- [66] M.-B. Madec, D. Crouch, G. R. Llorente, T. J. Whittle, M. Geoghegan, S. G. Yeates, *J. Mater. Chem.* **2008**, *18*, 3230.
- [67] J. H. Lee, H. H. Choi, Y. D. Park, J. E. Anthony, J. A. Lim, J. Cho, D. S. Chung, J. Hwang, H. W. Jang, K. Cho, W. H. Lee, *Adv. Funct. Mater.* **2018**, *28*, 1802875.
- [68] C. Teixeira da Rocha, K. Haase, Y. Zheng, M. Löffler, M. Hamsch, S. C. B. Mannsfeld, *Adv. Electron. Mater.* **2018**, *4*, 1800141.
- [69] M. R. Niazi, R. Li, E. Qiang Li, A. R. Kirmani, M. Abdelsamie, Q. Wang, W. Pan, M. M. Payne, J. E. Anthony, D.-M. Smilgies, S. T. Thoroddsen, E. P. Giannelis, A. Amassian, *Nat. Commun.* **2015**, *6*, 8598.
- [70] X. Wang, W. H. Lee, G. Zhang, X. Wang, B. Kang, H. Lu, L. Qiu, K. Cho, *J. Mater. Chem. C* **2013**, *1*, 3989.
- [71] S. Georgakopoulos, F. G. Del Pozo, M. Mas-Torrent, *J. Mater. Chem. C* **2015**, *3*, 12199.
- [72] H. Chung, Y. Diao, *J. Mater. Chem. C* **2016**, *4*, 3915.
- [73] Y. Diao, K. M. Lenn, W. Y. Lee, M. A. Blood-Forsythe, J. Xu, Y. Mao, Y. Kim, J. A. Reinspach, S. Park, A. Aspuru-Guzik, G. Xue, P. Clancy, Z. Bao, S. C. B. Mannsfeld, *J. Am. Chem. Soc.* **2014**, *136*, 17046.
- [74] A. Troisi, G. Orlandi, *J. Phys. Chem. B* **2005**, *109*, 1849.
- [75] P. S. Jo, D. T. Duong, J. Park, R. Sinclair, A. Salleo, *Chem. Mater.* **2015**, *27*, 3979.
- [76] S. Galindo, A. Tamayo, F. Leonardi, M. Mas-Torrent, *Adv. Funct. Mater.* **2017**, *27*, 1700526.
- [77] T. Salzillo, A. Campos, A. Babuji, R. Santiago, S. T. Bromley, C. Ocal, E. Barrena, R. Jouclas, C. Ruzie, G. Schweicher, Y. H. Geerts, M. Mas-Torrent, *Adv. Funct. Mater.* **2020**, *30*, 2006115.
- [78] A. Babel, S. A. Jenekhe, *Macromolecules* **2004**, *37*, 9835.
- [79] G. Lu, H. Tang, Y. Qu, L. Li, X. Yang, *Macromolecules* **2007**, *40*, 6579.
- [80] L. Qiu, X. Wang, W. H. Lee, J. A. Lim, J. S. Kim, D. Kwak, K. Cho, *Chem. Mater.* **2009**, *21*, 4380.
- [81] M. Chang, D. Choi, G. Wang, N. Kleinhenz, N. Persson, B. Park, E. Reichmanis, *ACS Appl. Mater. Interfaces* **2015**, *7*, 14095.
- [82] S. J. Rinehart, G. Yuan, M. D. Dadmun, *Soft Matter* **2020**, *16*, 1287.
- [83] L. Bu, M. Hu, W. Lu, Z. Wang, G. Lu, *Adv. Mater.* **2018**, *30*, 1704695.
- [84] G. Mattana, A. Loi, M. Woytasik, M. Barbaro, V. Noël, B. Piro, *Adv. Mater. Technol.* **2017**, *2*, 1700063.
- [85] X. Zhang, W. Deng, R. Jia, X. Zhang, J. Jie, *Small* **2019**, *15*, 1900332.
- [86] A. A. Jahnke, L. Yu, N. Coombs, A. D. Scaccabarozzi, A. J. Tilley, P. M. DiCarmine, A. Amassian, N. Stingelin, D. S. Seferos, *J. Mater. Chem. C* **2015**, *3*, 3767.
- [87] T. Marszalek, M. Li, W. Pisula, *Chem. Commun.* **2016**, *52*, 10938.
- [88] Y. Lei, P. Deng, J. Li, M. Lin, F. Zhu, T.-W. Ng, C.-S. Lee, B. S. Ong, *Sci. Rep.* **2016**, *6*, 24476.
- [89] I. Angunawela, M. M. Nahid, M. Ghasemi, A. Amassian, H. Ade, A. Gadisa, *ACS Appl. Mater. Interfaces* **2020**, *12*, 26239.
- [90] M. J. Ford, M. Wang, S. N. Patel, H. Phan, R. A. Segalman, T.-Q. Nguyen, G. C. Bazan, *Chem. Mater.* **2016**, *28*, 1256.
- [91] H.-R. Tseng, H. Phan, C. Luo, M. Wang, L. A. Perez, S. N. Patel, L. Ying, E. J. Kramer, T.-Q. Nguyen, G. C. Bazan, A. J. Heeger, *Adv. Mater.* **2014**, *26*, 2993.
- [92] A. T. Hidayat, H. Benten, N. Ohta, Y. Na, A. Muraoka, H. Kojima, M.-C. Jung, M. Nakamura, *Macromolecules* **2020**, *53*, 6630.
- [93] J. H. Lee, Y. H. Lee, Y. H. Ha, J. Kwon, S. Pyo, Y.-H. Kim, W. H. Lee, *RSC Adv.* **2017**, *7*, 7526.
- [94] P. Wei, X. Li, L. Wang, N. Liu, S. He, Y. Ren, Y. Zhu, Y. Yang, G. Lu, L. Bu, *Adv. Electron. Mater.* **2020**, *6*, 1901156.
- [95] C.-C. Shih, Y.-C. Chiang, H.-C. Hsieh, Y.-C. Lin, W.-C. Chen, *ACS Appl. Mater. Interfaces* **2019**, *11*, 42429.
- [96] M. Selivanova, C.-H. Chuang, B. Billet, A. Malik, P. Xiang, E. Landry, Y.-C. Chiu, S. Rondeau-Gagné, *ACS Appl. Mater. Interfaces* **2019**, *11*, 12723.
- [97] S. Nikzad, H.-C. Wu, J. Kim, C. M. Mahoney, J. R. Matthews, W. Niu, Y. Li, H. Wang, W.-C. Chen, M. F. Toney, M. He, Z. Bao, *Chem. Mater.* **2020**, *32*, 897.
- [98] H. Sirringhaus, M. Ando, *MRS Bull.* **2008**, *33*, 676.
- [99] M. Nikolka, I. Nasrallah, B. Rose, M. K. Ravva, K. Broch, A. Sadhanala, D. Harkin, J. Charmet, M. Hurhangee, A. Brown, S. Illig, P. Too, J. Jongman, I. McCulloch, J.-L. Bredas, H. Sirringhaus, *Nat. Mater.* **2017**, *16*, 356.
- [100] H. T. Nicolai, M. Kuik, G. A. H. Wetzelaer, B. de Boer, C. Campbell, C. Risko, J. L. Brédas, P. W. M. Blom, *Nat. Mater.* **2012**, *11*, 882.
- [101] J.-M. Zhuo, L.-H. Zhao, R.-Q. Png, L.-Y. Wong, P.-J. Chia, J.-C. Tang, S. Sivaramakrishnan, M. Zhou, E. C.-W. Ou, S.-J. Chua, W.-S. Sim, L.-L. Chua, P. K.-H. Ho, *Adv. Mater.* **2009**, *21*, 4747.
- [102] S. Hoshino, M. Yoshida, S. Uemura, T. Kodzasa, N. Takada, T. Kamata, K. Yase, *J. Appl. Phys.* **2004**, *95*, 5088.
- [103] C.-C. Liu, C.-M. Yang, W.-H. Liu, H.-H. Liao, S.-F. Horng, H.-F. Meng, *Synth. Met.* **2009**, *159*, 1131.
- [104] L. S. Cardoso, J. C. Stefanelo, R. M. Faria, *Synth. Met.* **2016**, *220*, 286.
- [105] D. Feili, M. Schuettler, T. Doerge, S. Kammer, T. Stieglitz, *Sens. Actuators, A* **2005**, *120*, 101.
- [106] T. Marszalek, M. Gazicki-Lipman, J. Ulanski, *Beilstein J. Nanotechnol.* **2017**, *8*, 1532.
- [107] S. Choi, J. W. Jeong, G. Jo, B. C. Ma, M. Chang, *Nanoscale* **2019**, *11*, 10004.
- [108] D. Chlebosz, Ł. Janasz, K. Janus, M. Gazińska, W. Goldeman, J. Ulanski, W. Pisula, A. Kiersnowski, *Dyes Pigm.* **2017**, *140*, 491.
- [109] X. Zhan, A. Facchetti, S. Barlow, T. J. Marks, M. A. Ratner, M. R. Wasielewski, S. R. Marder, *Adv. Mater.* **2011**, *23*, 268.
- [110] S. Zhao, J. Li, D. Cao, G. Zhang, J. Li, K. Li, Y. Yang, W. Wang, Y. Jin, R. Sun, C.-P. Wong, *ACS Appl. Mater. Interfaces* **2017**, *9*, 12147.
- [111] S. J. Benight, C. Wang, J. B. H. Tok, Z. Bao, *Prog. Polym. Sci.* **2013**, *38*, 1961.
- [112] S. Savagatrup, A. D. Printz, T. F. O'Connor, A. V. Zaretski, D. J. Lipomi, *Chem. Mater.* **2014**, *26*, 3028.
- [113] T. Q. Trung, N.-E. Lee, *Adv. Mater.* **2017**, *29*, 1603167.
- [114] Y. Wang, C. Zhu, R. Pfattner, H. Yan, L. Jin, S. Chen, F. Molina-Lopez, F. Lissel, J. Liu, N. I. Rabiah, Z. Chen, J. W. Chung, C. Linder, M. F. Toney, B. Murmann, Z. Bao, *Sci. Adv.* **2017**, *3*, e1602076.
- [115] K. Gu, J. W. Onorato, C. K. Luscombe, Y. Loo, *Adv. Electron. Mater.* **2020**, *6*, 1901070.
- [116] D. Choi, H. Kim, N. Persson, P.-H. Chu, M. Chang, J.-H. Kang, S. Graham, E. Reichmanis, *Chem. Mater.* **2016**, *28*, 1196.
- [117] J. I. Scott, X. Xue, M. Wang, R. J. Kline, B. C. Hoffman, D. Dougherty, C. Zhou, G. Bazan, B. T. O'Connor, *ACS Appl. Mater. Interfaces* **2016**, *8*, 14037.
- [118] D. Rodriguez, S. Savagatrup, E. Valle, C. M. Proctor, C. McDowell, G. C. Bazan, T.-Q. Nguyen, D. J. Lipomi, *ACS Appl. Mater. Interfaces* **2016**, *8*, 11649.
- [119] G. Zhang, M. McBride, N. Persson, S. Lee, T. J. Dunn, M. F. Toney, Z. Yuan, Y.-H. Kwon, P.-H. Chu, B. Ristein, E. Reichmanis, *Chem. Mater.* **2017**, *29*, 7645.
- [120] M. Shin, J. Y. Oh, K.-E. Byun, Y.-J. Lee, B. Kim, H.-K. Baik, J.-J. Park, U. Jeong, *Adv. Mater.* **2015**, *27*, 1255.

- [121] F. Ge, Z. Liu, S. B. Lee, X. Wang, G. Zhang, H. Lu, K. Cho, L. Qiu, *ACS Appl. Mater. Interfaces* **2018**, *10*, 21510.
- [122] K. Yu, B. Park, G. Kim, C.-H. Kim, S. Park, J. Kim, S. Jung, S. Jeong, S. Kwon, H. Kang, J. Kim, M.-H. Yoon, K. Lee, *Proc. Natl. Acad. Sci. U.S.A.* **2016**, *113*, 14261.
- [123] J. Xu, S. Wang, G.-J. N. Wang, C. Zhu, S. Luo, L. Jin, X. Gu, S. Chen, V. R. Feig, J. W. F. To, S. Rondeau-Gagné, J. Park, B. C. Schroeder, C. Lu, J. Y. Oh, Y. Wang, Y. Kim, H. Yan, R. Sinclair, D. Zhou, G. Xue, B. Murmann, C. Linder, W. Cai, J. B.-H. Tok, J. W. Chung, Z. Bao, *Science* **2017**, *355*, 59.
- [124] J. Y. Oh, D. Son, T. Katsumata, Y. Lee, Y. Kim, J. Lopez, H.-C. Wu, J. Kang, J. Park, X. Gu, J. Mun, N. G.-J. Wang, Y. Yin, W. Cai, Y. Yun, J. B. H. Tok, Z. Bao, *Sci. Adv.* **2019**, *5*, eaav3097.
- [125] S. Zhang, Y. Cheng, L. Galuska, A. Roy, M. Lorenz, B. Chen, S. Luo, Y. Li, C. Hung, Z. Qian, P. B. J. St Onge, G. T. Mason, L. Cowen, D. Zhou, S. I. Nazarenko, R. F. Storey, B. C. Schroeder, S. Rondeau-Gagné, Y. Chiu, X. Gu, *Adv. Funct. Mater.* **2020**, *30*, 2000663.
- [126] M. Xu, L. Xiang, T. Xu, W. Wang, W. Xie, D. Zhou, *Appl. Phys. Lett.* **2017**, *111*, 183302.
- [127] H. Chen, W. Zhang, M. Li, G. He, X. Guo, *Chem. Rev.* **2020**, *120*, 2879.
- [128] Y.-C. Chiang, C.-C. Shih, S.-H. Tung, W.-C. Chen, *Polymer* **2018**, *155*, 146.
- [129] Y.-H. Cheng, A.-N. Au-Duong, T.-Y. Chiang, Z.-Y. Wei, K.-L. Chen, J.-Y. Lai, C.-C. Hu, C.-C. Chueh, Y.-C. Chiu, *ACS Omega* **2019**, *4*, 22082.
- [130] X. Zhang, B. Wang, L. Huang, W. Huang, Z. Wang, W. Zhu, Y. Chen, Y. Mao, A. Facchetti, T. J. Marks, *Sci. Adv.* **2020**, *6*, eaaz1042.
- [131] Z.-P. Yu, C.-H. Ma, Q. Wang, N. Liu, J. Yin, Z.-Q. Wu, *Macromolecules* **2016**, *49*, 1180.
- [132] X. Wu, S. Mao, J. Chen, J. Huang, *Adv. Mater.* **2018**, *30*, 1705642.
- [133] Y. Wang, Q. Gong, Q. Miao, *Mater. Chem. Front.* **2020**, *4*, 3505.
- [134] S. G. Surya, H. N. Raval, R. Ahmad, P. Sonar, K. N. Salama, V. R. Rao, *TrAC, Trends Anal. Chem.* **2019**, *111*, 27.
- [135] X. Zhang, B. Wang, W. Huang, G. Wang, W. Zhu, Z. Wang, W. Zhang, A. Facchetti, T. J. Marks, *Nano Lett.* **2019**, *19*, 471.
- [136] S. Hou, J. Yu, X. Zhuang, D. Li, Y. Liu, Z. Gao, T. Sun, F. Wang, X. Yu, *ACS Appl. Mater. Interfaces* **2019**, *11*, 44521.
- [137] W. H. Lee, H. H. Choi, D. H. Kim, K. Cho, *Adv. Mater.* **2014**, *26*, 1660.
- [138] L. Feng, W. Tang, J. Zhao, R. Yang, W. Hu, Q. Li, R. Wang, X. Guo, *Sci. Rep.* **2016**, *6*, 20671.
- [139] J. H. Lee, Y. Seo, Y. D. Park, J. E. Anthony, D. H. Kwak, J. A. Lim, S. Ko, H. W. Jang, K. Cho, W. H. Lee, *Sci. Rep.* **2019**, *9*, 21.
- [140] S. H. Kim, W. M. Yoon, M. Jang, H. Yang, J.-J. Park, C. E. Park, *J. Mater. Chem.* **2012**, *22*, 7731.
- [141] J. Huang, J. Du, Z. Cevher, Y. Ren, X. Wu, Y. Chu, *Adv. Funct. Mater.* **2017**, *27*, 1604163.
- [142] D. Ljubic, W. Liu, C. E. González-Espinoza, N.-X. Hu, Y. Wu, S. Zhu, *Adv. Electron. Mater.* **2017**, *3*, 1700284.
- [143] D. Ljubic, W. Liu, N.-X. Hu, Y. Wu, S. Zhu, *Org. Electron.* **2018**, *59*, 349.
- [144] S. Y. Yeo, S. Park, Y. J. Yi, D. H. Kim, J. A. Lim, *ACS Appl. Mater. Interfaces* **2017**, *9*, 42996.
- [145] S. Han, X. Zhuang, W. Shi, X. Yang, L. Li, J. Yu, *Sens. Actuators, B* **2016**, *225*, 10.
- [146] X. Wang, Z. Liu, S. Wei, F. Ge, L. Liu, G. Zhang, Y. Ding, L. Qiu, *Synth. Met.* **2018**, *244*, 20.
- [147] S. Wei, F. Tian, F. Ge, X. Wang, G. Zhang, H. Lu, J. Yin, Z. Wu, L. Qiu, *ACS Appl. Mater. Interfaces* **2018**, *10*, 22504.
- [148] B. Li, G. Sauv e, M. C. Iovu, M. Jeffries-EL, R. Zhang, J. Cooper, S. Santhanam, L. Schultz, J. C. Revelli, A. G. Kusne, T. Kowalewski, J. L. Snyder, L. E. Weiss, G. K. Fedder, R. D. McCullough, D. N. Lambeth, *Nano Lett.* **2006**, *6*, 1598.
- [149] L.-Z. Qiu, S.-Y. Wei, H.-S. Xu, Z.-X. Zhang, Z.-Y. Guo, X.-G. Chen, S.-Y. Liu, D. Wu, L.-B. Luo, *Nano Lett.* **2020**, *20*, 644.
- [150] W.-Y. Kong, G.-A. Wu, K.-Y. Wang, T.-F. Zhang, Y.-F. Zou, D.-D. Wang, L.-B. Luo, *Adv. Mater.* **2016**, *28*, 10725.
- [151] S. Wu, G. Wang, Z. Xue, F. Ge, G. Zhang, H. Lu, L. Qiu, *ACS Appl. Mater. Interfaces* **2017**, *9*, 14974.
- [152] Q. Wang, S. Wu, F. Ge, G. Zhang, H. Lu, L. Qiu, *Adv. Mater. Interfaces* **2016**, *3*, 1600518.
- [153] X. Wang, F. Zhao, Z. Xue, Y. Yuan, M. Huang, G. Zhang, Y. Ding, L. Qiu, *Adv. Electron. Mater.* **2019**, *5*, 1900174.



Lukasz Janasz obtained his M.Sc. in Technical Physics from the AGH University of Science and Technology in 2013. In 2014, he joined Prof. Jacek Ulanski's group at the Lodz University of Technology working on organic electronics. The focus of his investigation was ambipolar organic field-effect transistors with ultrathin semiconducting films. During his research, he cooperated with Prof. Klaus M ullen's group from the Max Planck Institute for Polymer Research. He obtained his Ph.D. in 2018. Currently, he holds the position of research and development engineer in Corning Optical Communication, Poland.



Michal Borkowski was born in Tomaszów Mazowiecki, Poland in 1993. He received his M.Sc. in Nanotechnology in 2017 from the Lodz University of Technology in Poland. Specializing in polymer sciences, he realized his M.Sc. thesis and started his Ph.D. studies in Chemical Technology in the Department of Molecular Physics. His research is focused on the fabrication and characterization of organic field-effect transistors. Currently, he works on polymer phase separation during thermocapillary instabilities for OFET active layer application. Simultaneously, he holds the position of regulatory affairs specialist in the medical device company HTL-STREFA S.A.



Tomasz Marszalek joined the group of Professor Jacek Ulanski at the Department of Molecular Physics, where he completed his dissertation in 2012 (Chemical Technology). After postdoctoral positions in the group of Prof. Klaus Müllen at the Max Planck Institute for Polymer Research (MPIP) and Prof. Uwe Bunz at the Ruprecht-Karls-Universität Heidelberg, he developed his first own independent research group (First Team program of the Foundation of Polish Science) which focuses on π -conjugated self-organizing systems and their potential application in organic electronic field. In January 2018, he additionally joined the Department of Molecular Electronics of MPIP as a group leader.



Wojciech Pisula gained his PhD in Chemistry at the Max Planck Institute for Polymer Research in 2005 and took over the position as project leader. In 2015, he received his habilitation in Material Science at the Technical University of Darmstadt. He became Associate Professor in 2015 and Full Professor in 2020 in the Department of Molecular Physics at the Lodz University of Technology. Since 2016 he is editor for Synthetic Metals and since 2020 Editor-in-Chief for Electronic Materials. Parallel to his academic career, he joined Evonik Industries in 2006 where he is currently Director at the Applied Technology Silicone.